UNIVERSIDADE DE LISBOA
FACULDADE DE CIÊNCIAS
DEPARTAMENTO DE FÍSICA

Synchronization of a binary mixture of coupled Brownian oscillators

Gonçalo Santos Paulo

Mestrado em Física
Especialização em Física Estatística e Matéria Condensada

Dissertação orientada por:
Dr. Mykola Tasinkevych

2020

Acknowledgements

I would like to thank my supervisor Mykola Tasinkevych, and my roommates, Pedro Didier and Vasco Braz for helping me along the way with their wisdom and their patience. I would also like to thank my mother Isaura, my father Hirondino and my sister Ema for all the support while I was in college and whilst finishing this work. And a special thanks to Maria and all the hours she spent waiting for me to let go of my computer. I acknowledge all the financial support from the Portuguese Foundation for Science and Technology (FCT) under Contract Nos. IF/00322/2015 and UID/FIS/00618/2019.

Abstract

Synchronization phenomena have been studied for a long time and are present in many natural and artificial systems. They are the key phenomena in areas like biology, neurosciences and condensed matter physics. In our work we try to understand the synchronization behaviour of a binary mixture of moving oscillators. We established a working framework to model synchronization phenomena, implementing the Kuramoto model and with this framework we confirmed some of the theoretical results of this theory. We used a computational library to perform Langevin dynamics and then modified the Kuramoto model to apply it to a binary mixture of Brownian particles. The synchronization interaction of this binary mixture can be modeled in numerous ways, thus we studied two different models. In Model I we split our oscillators into two groups where similar particles had a positive coupling constant, which lead them to phase lock with phase difference 0, and two different particles had a negative coupling constant, which lead them to phase lock with a phase difference of π. Model II consists of a mixture of oscillators where one type of oscillators has a negative coupling constant in all its interactions, these being called contrarian oscillators, and the other type has a positive coupling with similar oscillators and a negative coupling with the other type. We also applied model I to active Brownian particles, in a similar way to the continuous Vicsek model, to connect this model to some phenomena that can be observed in nature.

We explored a broad range of parameters for these models. We looked at different splits of the mixture, from 5% to 95%, at different coupling constant ranges, but we considered that all oscillators have the same internal phase frequency and that the range of interaction is constant.

Model I enhances synchronization for particles of both groups, allowing control over the synchronization behaviour by changing the interaction strength and the mixture split percentage. Model II can enhance synchronization for the contrarians, which would not synchronize if they were left alone, and can suppress synchronization for both oscillator groups if their interaction is strong enough. The ability for the oscillators to move and exchange neighbours increases the synchronization speed, as was observed when active Brownian particles were used.

Keywords: Synchronization, Brownian particles, Complex Networks, Complex Systems

Resumo

Fenómenos de sincronização estão presentes em muitos sistemas naturais e artificiais, e são o fenómeno chave no estudo de alguns destes sistemas. É possível observar fenómenos de sincronização em ecologia, por exemplo nas oscilações de presa e predador; na etologia com a sincronização de coros de sapos e do piscar de pirilampos; na fisiologia, na sincronização de ritmos biológicos, como o ciclo circadiano e alguns ciclos hormonais; na matéria condensada, na sincronização de osciladores de spin Hall; e em tantos outros sistemas. A compreensão de fenómenos de sincronização, e o estudo de modelos de sincronização são portanto campos bastante ativos atualmente.

Estabelecemos um modelo de trabalho para estudar o fenómeno de sincronização. Primeiro estudamos o modelo de Kuramoto, um modelo usado para estudar sincronização desde 1975. Este modelo consiste num sistema de equações diferencias, não lineares e autónomas, que regem a evolução da fase de cada oscilador que modelam. Kuramoto introduziu alguns resultados analíticos sobre o modelo e desde então ele tem sido cada vez mais usado e novas técnicas foram desenvolvidas. A outra base do nosso modelo de trabalho são as partículas brownianas, ou seja partículas que por estarem imersas num fluído têm um movimento aleatório dentro dele. O estudo das partículas Brownianas também já tem muita história existindo uma grande quantidade de resultados teóricos e experimentais sobre elas. Usamos alguns dos resultados teóricos mais conhecidos para validarmos o código que usamos para este trabalho. Neste trabalho utilizamos o LAMMPS, uma biblioteca em C++ para desenvolver algoritmos de dinâmica molecular e modelos coarse-grained. e tivemos que implementar de raiz a interação de Kuramoto para as nossas partículas. Esta biblioteca permite realizar simulações moleculares em paralelo e o nosso código passou em todos os testes teóricos.

O nosso objectivo era estudar como se dava a sincronização de uma mistura de osciladores, que interagiam com os seus vizinhos e que se deslocavam no espaço como particulas Brownianas. Assim, modificamos o modelo de Kuramoto para aplicá-lo a uma mistura binária de partículas Brownianas. A interação de sincronização dessa mistura binária pode ser modelada de várias maneiras e estudamos dois modelos diferentes.

No Modelo I, dividimos os osciladores em dois grupos onde partículas semelhantes tinham uma constante de acoplamento positiva, o que leva a que a fase desses osciladores evolua para que fiquem com uma diferença de fase de 0. Se os osciladores fossem de dois tipos diferentes as partículas tinham uma constante de acoplamento negativa, o que conduz a uma diferença de fase de π. Chamamos a este modelo o modelo de osciladores repulsivos visto que os osciladores de tipos diferentes tendem a ficar com a fase desfasada por π. Estávamos interessados em controlar a sincronização e em saber se era possível acelerá-la, retardá-la ou até mesmo impedi-la. Para isso estudamos neste modelo o papel de diferentes constantes de acoplamento, de diferentes percentagem para a mistura de osciladores, de diferentes densidades do sistema de osciladores, e verificamos que apesar de ser impossível impedi-la é possível acelerá-la e retardá-la.

O Modelo II consiste numa mistura de osciladores onde um tipo de oscilador possui uma constante de acoplamento negativa em todas as suas interações, sendo estes denominados osciladores “contrariados”, e o outro tipo possui acoplamento positivo com osciladores semelhantes e acoplamento negativo com o outro tipo. Com este modelo foi possível impedir a sincronização de partículas e estudamos o efeito da quantidade de osciladores contrariados e também o papel da constante de acoplamento negativo. Este resultado é interessante devido às possíveis aplicações em situações onde a sincronização é um fenómeno indesejado, como a sincronização do disparo dos neurónios num paciente com epilepsia ou Parkinson.

Estendemos ainda ambas as modificações ao modelo de Kuramoto para partículas brownianas ativas, de forma semelhante ao modelo contínuo de Vicsek, para conectar este modelo a alguns fenômenos que podem ser observados na natureza. O modelo de Vicsek foi extensamente usado na caracterização de fenomenos de deslocação colectivos. Com ele é possível explicar e prever as trajetórias observadas nos voos de conjuntos de pássaros ou no deslocamento de cardumes. O uso do modelo de Kuramoto como interação entre as partículas ativas permitiu observar alguns dos fenomenos previstos por Vicsek, como os engarrafamentos, onde as colisões das partículas geram aglomerados, e permitiu nos colocar questões sobre possíveis trabalhos próximos. Foi possível observar que a velocidade de propulsão das partículas contribui para o processo de sincronização, confirmando a importância da capacidade de mistura entre os osciladores para que a sincronização se processe mais rápido.

Palavras-chave: Sincronização, Particulas Brownianas, Redes Complexas, Sistemas Complexos

Contents

List of Figures **xi**

1 Introduction **1**

2 Kuramoto Model **3**
2.1 Mean-field continuous solution . . . 3
2.2 Examples . . . 9
2.3 Simulations . . . 10

3 Brownian Motion **15**
3.1 Analytic Results . . . 15
3.2 Examples . . . 17
3.3 Simulations . . . 19

4 Models for a binary mixture of Brownian oscillators **23**
4.1 Model I - Repulsive interaction . . . 23
4.2 Model II - Contrarian oscillators . . . 31

5 Active Brownian Motion **35**
5.1 Analytic results . . . 35
5.2 Examples . . . 36
5.3 Simulations . . . 37

6 Active model I: a model for a binary mixture of active Brownian oscillators **39**

7 Conclusion and future work **43**

Bibliography **45**

List of Figures

2.1 **Second order phase transition of the Kuramoto model.**For the Cauchy distribution of frequencies the Kuramoto model the order parameter is 0 below a critical value of K,K_C and above K_C, r behaves like $r = \sqrt{1 - \frac{K_c}{K}}$ 7

2.2 **Application of the Kuramoto model in steering agents.** Panel (a) illustrates the particle kinematics (6). Panels (b)-(e) illustrate the controlled dynamics, eq. (2.26) with n=6 particles, a complete interaction graph, and identical and constant natural frequencies: ω_i(t) = 0 for all agents in panels (b) and (c) and ω_i(t) = 1 for all agents in panels (d) and (e). The values of K are $K = 1$ in panel (b) and (d) and K=1 in panel (c) and (e). The arrows depict the orientation, the dashed curves show the long-term position dynamics, and the solid curves show the initial transient position dynamics. As illustrated, the resulting motion displays "synchronized" or "balanced" heading angles for $K = 1$, and translational motion for ω_i(t) = 0, respectively circular motion for ω_i(t) = 1. Taken with permission from [1]. 9

2.3 **Application of the Kuramoto model in networks of neurons.**Order parameter magnitude as a function of the coupling strength for a network of Rulkov neurons (black: uniform, red: Cauchy) and Kuramoto oscillators (green: uniform, blue: Cauchy) with N = 1000 nodes, for (a) global coupling, (b) Erdös–Rényi; (c) small-world, and (d) scale-free. Taken with permission from [2] 10

2.4 **Evolution of the order parameter.** Panels (a),(b),(d),(e) represent system of oscillators at a given time. The position of each red point in the unit circle is given by the phase of a specific oscillator and the position of the black point is given by the complex order parameter $re^{i\Psi(t)}$, equation 2.2. (a) and (d) show the initial configuration of the system with N = 500, and $g(\omega_i)$ the Dirac distribution, $\delta(\omega)$. The initial phases were drawn from an uniform distribution in the interval [0;2π]. The value of K is -1 and 1 respectively. (b) and (e) are the systems in (a) and (d) after 10000 timesteps, (c) and (f) corresponds to the time evolution of the value of r, the order parameter. The time evolution for this distribution can be solved analytically and is given by equation (2.24), which is represented as the dashed red line in the plot. In (c) the system remains not synchronized, $r \sim 0$, even after long time periods because the value of K is smaller than the critical value that allows for synchronization, which for this system is $K_C = 0$ In (f) the system synchronizes,$r \sim 1$, and remains phase-locked because the value of K is higher than the critical value of for synchronization, $K_C = 0$, for this system. 12

2.5 **Phase drifting and phase locking.** (a) and (c) shows the final configuration of a system of 200 oscillators, with a standard Cauchy distribution of frequencies after 50000 and 10000 timesteps respectively. The values of K were 1 for (a) and 3 for (b) The initial phases were drawn from an uniform distribution in the interval [0;2π]. The position of each red point in the unit circle is given by the phase of a specific oscillator and the position of the black point is given by the complex order parameter $re^{i\Psi(t)}$, equation 2.2. The green triangle and the blue square represent 2 oscillators chosen at random. (b) and (d) show the evolution of the difference of the chosen oscillators phase and $\Psi(t)$ in their respective colors. In (b) it is possible to observe the phase drift of the randomly chosen oscillators as their phase changes non uniformly. This system is does not synchronize because the value of K is below its critical value for synchronization, $K_C = 2$. In (d) we observe the phase-locking that is a characteristic of synchronization, with the phase difference of each oscillator staying constant in time. Synchronization is possible because value of K is larger than the critical value for synchronization, $K_C = 2$ 13

2.6 **Synchronization phase transition.** The nature of the Kuramoto phase transition depends on the distribution of the frequency distribution of its oscillators and also on the geometry. For the standard Cauchy distribution this transition is a second order phase transition. Below K_C the only stable steady state solution is $r = 0$, but above K_C this solution becomes unstable and the stable steady state solution becomes $r = \sqrt{1 - \frac{K_C}{K}}$ as shown in panel (a). The simulations are done for N = 500, the value of r_∞ of does not exactly match up with the theoretical behaviour for $N \to \infty$. Panel (b) shows the first order phase transition characteristic of the Dirac distribution for the oscillators frequency. The simulations are done for N = 500 and the values close to the critical point do not correspond to the theoretical results due to the long simulation times needed for the system to reach its stationary value. 14

2.7 **Dependence of the r(t) curve parameters on K.** The value of the growth rate, κ, is equal to the value of K for the Dirac distribution of frequencies, $g(\omega) = \delta(\omega)$. The simulations match up with the theoretical result as we can observe in panel (a). The value of the timesift, t_0, is inversely proportional to the value of K for the Dirac distribution of frequencies, $g(\omega) = \delta(\omega)$.The simulations match up with the theoretical result as can be observed in panel (b). All the simulations were done with $N = 300$ 14

3.1 **Formation of micels by anphiphilic molecules.** By varying the ration between the temperature, T and the strength of the hydrophilic interaction, ϵ it is possible to control the formation of vesicles. Figure taken with permission from [3]. 17

3.2 **Brownian particle in an optical trap**. (a) Trajectory of a Brownian particle in an optical trap. The particle explores an ellipsoidal volume around the center of the trap, as evidenced by the shaded area which represents an equiprobability surface. (b) and (c) The probability distributions of finding the particle in the z- and y-planes follow a twodimensional Gaussian distribution around the trap center. Taken with permission from [4]. 18

3.3 **Dependence of the diffusion constant with packing fraction.** As the packing fraction increases, and due to the steric interaction between particles, their mobility decreases and that is captured by the decrease of the diffusion constant measured in the system. 20

3.4 **Proprieties of a Brownian particle.** In panel (a) we can see the trajectories of a Brownian particle moving in a 50x50 box with periodic conditions. As can be observed the trajectory seems random and with no discernible pattern while exploring space. It is not possible to know the initial condition just by looking into the trajectory, as the system has no memory. In panel (B) the mean square displacement (MSD) of a Brownian particle, $\langle (x(t^*) - x(0))^2 \rangle$, grows linearly in time, with the slope being equal to $2D$, D being the diffusion coefficient, equation (3.7). Panel (c) shows simulations with $damp = 1$(green) and $damp = 5$(blue) and how they match up with the theoretical results(dashed colored lines), showing that increasing damp decreases the value of the diffusion constant, D, as it is related to increasing the friction constant γ. In panel (d) we see that increasing the value of temperature increases the value of the diffusion constant, D, as how the simulations with $T = 1$(green) and $T = 5$(blue) match with the theoretical results (dashed colored lines). 21

4.1 **Time evolution of the order parameter.** Panels (a) and (c) show the time evolution of the order parameter for systems with N = 1800, $\phi = 0.5$, $K = 0.001$ and $H = -0.001$ and -0.1 respectively. The red curve is the fitted curve for $r(t^*) \sim \frac{1}{\sqrt{1+e^{-\kappa(t^*-t_0)}}}$. Panels (b) and (d) show the time evolution of $1 - r$, highlighting the late time $r(t^*) \sim 1 - e^{-\frac{t*}{\tau}}$.Panel (a) shows how different initial conditions give the same qualitatively behaviour while (c) shows that each initial condition has a different behaviour qualitatively. Panels (b) and (d) show how the late time behaviour is similar for all initial conditions. . 25

4.2 **Snapshots of the time evolution of the system.** Panels (a) and (e) show the time evolution of the order parameter for systems with N = 1800, $\phi = 0.5$, $K = 0.001$ and $H = -0.001$ and -0.1 respectively. Panels (b) to (d) show the same system of panel (a) with each panel being at the time respective to the dashed lines in panel (a), and panels (f) to (h) show the same system of panel (e) with each panel being at the time respective to the dashed lines in panel (e). The color scheme used for the phase to the oscillators is chosen as to better display the vortices observed. Both systems reach a synchronized state, $r \sim 1$, and an almost uniform coloring is observed in panels (d) and (h). 26

4.3 **Dependence of κ and t_0 on ϕ.** Panel (a) shows the dependence of κ on ϕ for various values of ζ, by varying the value of H. Panel (b) shows the dependence of t_0 on ϕ for various values of ζ, by varying the value of H. In all cases, $K = 0.001$ and $N = 1800$. . 26

4.4 **Dependence of κ and t_0 on ζ.** Panel (a) shows the dependence of κ on ζ for various values of ϕ. Panel (b) shows the dependence of t_0 on ζ for various values of ϕ in a log-log scale, In all cases, $K = 0.001$ and $N = 1800$. 27

4.5 **Snapshots of some systems.** The snapshots show the time evolution of the system from (1) to (3)(t^* = 200, t^*=1500, t^*=3500 respectively). Different letters have the same initial conditions but different parameters: (A) has $\zeta = 20$, $\eta = 0.56$, $\phi = 0$, (B) has $\zeta = 20$, $\eta = 0.56$, $\phi = 0.5$,(C) has $\zeta = 0.1$, $\eta = 0.56$, $\phi = 0.5$, (D) has $\zeta = 20$, $\eta = 0.14$, $\phi = 0.5$ and in all cases N=7200. 28

4.6 **Dependence of τ on ϕ and ζ.** Panel (a) shows that the synchronization characteristic time, τ increases as a function of ϕ. It is symmetrical at $\phi = 0.5$ decreasing to the same value for values of $\zeta < 1$. For values of $\zeta > 1$ the opposite is true, decreasing as a function of ϕ until $\phi = 0.5$, after that increasing to close its starting value. When $|H| = K$ τ doesn't depend on ϕ. Panel (b) shows that when $\zeta > 10, \tau \propto \zeta^{\alpha(\phi)}$. The dependence of α on ϕ is shown in the inset.In all cases, $\eta = 0.14$, $N = 1800$, $K = 0.1$. . . 29

4.7 **Characteristic time dependence on η.** Panel (a) shows that if the characteristic time is rescaled by N it is possible to observe the same dependence of $\frac{\tau}{N}$ with η. In panel (b) we see that for the same ζ, N and ϕ but different η the system has a packing fraction that minimizes τ, due to the balance of short range interactions and mixing capability 29

4.8 **Dependence of t_c with ϕ and ζ.** Panel (a) shows the dependence of t_c on ϕ for various values of ζ, by varying the value of H. Panel (b) shows the dependence of t_c on ζ for various values of ϕ. For all cases $K = 0.1$ and $N = 1800$. 30

4.9 **Time evolution of the order parameters for model II.** Panel (a) shows the value of the order parameter for particles of type A and panel (b) shows the value of the order parameter for particles of type B. For values of $|H| < 0.1$ synchronization happens like in model I, the system fully synchronizing after a given time. For values of $|H| > 0.1$ both A and B particles reach a saturation value, r_∞ smaller than 1, the system never fully synchronizing. For even larger values of $|H|$, $|H| = 10$, the order parameter behaves erratically and the system never synchronizes. All simulations were done with $K = 0.001$ and $\phi = 0.5$ 32

4.10 **Phase diagram for the value of r_∞.**Panel (a) shows the value of r_∞ for particles of type A and panel (b) shows the value of r_∞ for particles of type B. It is possible to observe a continuous configurational transition as the value of r_∞ goes from 1 to 0. The value of r_∞ is different for particles of type A, panel (a) and for particles of type B, panel (b) and the values of ζ or ϕ that suppress their synchronization are lower for particles of type B. All simulations were done with $K = 0.1$. 32

4.11 **Dependence of $r_{a\infty}$ and $r_{b\infty}$ on ϕ.** In panel (a) we see the decrease of $r_{a\infty}$ as ϕ increases. In panel (b) we see the same decrease of $r_{b\infty}$ as ϕ increases. In both cases $N = 1800$, $H = -1$ and $K = 0.1$. 33

4.12 **Snapshots of the time evolution of Model II.** Panels (a)-(l) show snapshots with particles A and B separated, top and bottom plot respectively, to better distinguish their behaviour. Plots (a)-(c) show synchronization of the particles of type A, $r = 0.39$, 0.8 and 0.9 respectively, while the particles of type B remain unsynchronized, $r < 0.4$ in panels (d)-(f), due to the small value of H, $H = -0.001$. Plots (g)-(h) show how high values of $|H|$, $H = -10$, completely stop synchronization from happening as the value of r fluctuates for particles of both types, going as high as 0.38 but staying around $r = 0.2$. For all, $K = 0.1$, $N = 1800$ and $\phi = 0.1$ 34

5.1 A schematic illustrating self-electrophoresis. Hydrogen peroxide is oxidized to generate protons in solution and electrons in the wire on the Pt end. The protons and electrons are then consumed with the reduction of H_2O_2 on the Au end. The resulting ion flux induces motion of the particle relative to the fluid, propelling the particle toward the platinum end with respect to the stationary fluid. Taken with permission from [5]. 36

5.2 Living crystals formed by clusters: due to the motility of theseJanus particles it is possible to observe a phase segregation into the dense, crystal-like phase, and the dilute, gas-like phase. Taken with permission from [6]. 37

5.3 **Behaviour of a active Brownian particle.**In panel (a) we can see the trajectories of an active Brownian particle moving in a 50x50 box with periodic conditions. In panel (B) the mean square displacement (MSD) of a Brownian particle, $\langle (x(t^*) - x(0))^2 \rangle$, grows linearly in time, with the slope being equal to $2D$, D being the diffusion coefficient, equation (3.7), after a ballistic regimen where the mean square displace grows quadractically in time. Panel (c) shows simulations with $vp = 10$(green) and $vp = 1$(blue) and how they match up with the theoretical results(dashed colored lines), showing that increasing the propulsion velocity, v_p, increases the value of the diffusion constant, D, according to equation 5.3). 38

6.1 **Time evolution of the order parameter and the dependence of t_c.** Panel (a) shows the dependence of r with the value of v_p and how the activity of the particle changes the way it synchronizes, the order parameter no longer continuously growing do to existence of a rotational diffusion coefficient, D_θ. There is a non monotone dependence of t_c with v_p that may be due to the way the particles spatially distribute before synchronizing. 40

6.2 **Snapshots of clustering of active particles.** Panels (a)-(d) and (e)-(h) show the system configuration when the order parameter is 0.05, 0.30, 0.65, 0.95, respectively. We can see that in panels (a)-(d) there is no clustering, as the propulsion velocity of the particles is too low, $v_p = 0.1$. Panels (e)-(h) correspond to $v_p = 1$ and show that in intermediate times, while the system is not still synchronized, $r < 0.9$, it is possible to observe clustering . The cluster seen in (g) dissipates when the system is synchronized (h), due to the particles moving together and longer jamming together. 41

Chapter 1

Introduction

When Christian Huygens was looking at two pendulum clocks that were hanging from a common support he noticed that their pendulums moved in sync and that when he put them in opposite sides of the room they would become out of sync and never synchronize again. He was probably the first scientist who described the synchronization of two oscillators and since then there exist extensive studies on synchronization.

On a much bigger scale, the synchronization of swarms of fireflies amazed scientists for years as reports from Asian and Africa arrived to Europe telling tales of ”a great belt of light, some ten feet wide, formed by thousands upon thousands of fireflies whose green phosphorescence bridges the shoulder-high grass” [7] and that were answered with scepticism from the scientific community as an impossible phenomena and given various explanations not related with synchronization.

The study of these ordered phenomena in a world ruled by thermodynamics, which dictates that disorder is the final degenerate state of the universe, has attracted scientists for a long time, and synchronization being no exception, is a very active field of research and its phenomena are found in ecology, on the synchronization of frog choirs [8]; firefly blinking [9]; on neurosciences with the firing of neurons [10]; in physiology with biological rhythms [11]; in the swimming of bacteria [12]; in nanophysics, with the synchronization of mechanical nanodevices [13]; in hard condensed matter physics, with spin Hall nano-oscillators [14]; in sociology, when people clap their hands together [15]; and there even exists works on hindering and stopping synchronization when it is unwanted [16].

Synchronization can be thought about as the ”adjustment of rhythms of oscillating objects due to their weak interaction” [17] and this definition requires us to understand what are oscillating objects, what is an interaction between oscillators, what is the rhythm of an oscillating object and how can this rhythm be adjusted. The most interesting oscillating objects are self-sustained oscillators, oscillators which can sustain their natural rhythm due to some internal energy source and that are normally stable to small perturbations, returning to their original rhythm when left by themselves. These oscillators can be modeled by mathematical objects, called limit-cycle oscillators, that are normally described by autonomous, non-linear, differential equations. A limit-cycle is a closed trajectory in the phase-space of an oscillator meaning that the oscillator has a well defined periodic behaviour. An autonomous, non-linear, differential equations is a non-linear differential equations that does not explicitly depend on time.

Understanding how we can enhance and/or hinder synchronization to control it is a very sought after result, potentially leading to the cure for Parkinson [18] [19] [20] by understanding how neurons in the brain synchronize and what can be done to stop it. It can also mean controlling the movement of bacteria [12] or swarms/herds of animals [21] by controlling the oscillatory nature of these collective motion.

In this work we studied how synchronization is affected by the addition of movement and a new kind of synchronization interaction, one where oscillators do not try to align their phases but instead try to have a phase difference of π radians. We studied two different models for this interaction and try to determine what parameters enhance, hinder or kill synchronization. It is possible to apply the Kuramoto model to study the synchronization in any kind of network. For networks that are static it is possible to hinder synchronization by introducing, on the highest connectivity nodes, a small fraction, around 15%, of contrarian oscillators, oscillators that try to anti-align with other oscillator [16]. Take a fixed network of oscillators that is composed of two disconnected sub-networks. In this example it is trivial that this network would never synchronize because the sub networks would be independent[22]. By allowing this network to change in time, by some mechanism that would change its topology, it is possible for this set of oscillators to synchronize, contrary to what would happen if the network stayed fixed and disconnected. Allowing for the network to change in time, e.g. by allowing the oscillators to move and change neighbours, thus makes synchronization possible even in networks that originally were disconnected [23, 24]. The study of active particles [25] shows the importance of motility and how decreasing the mixing time is important for the speed up of synchronization. It also shows how there is a non-monotonic dependence of the synchronization rate on the motility when excluded volume interactions are taken into account. Designing the interaction between particles to attract or repel, based on their phases, provides an opportunity to control their collective behaviour, including full synchronization, spatial segregation by phases and even phase waves, as shown in [26]. To understand synchronization we started by explaining what the Kuramoto model is and what are some of its proprieties as we will be using it in all this work.

Chapter 2

Kuramoto Model

The Kuramoto model [27] is used to study synchronization phenomena [28, 29] and allows us to understand both dynamic and static networks of interacting oscillators. It was first introduced in 1975 by Yoshiki Kuramoto [27] and his work expanded on the earlier work on synchronization by Winfree in 1967 [30]. This model gives us an equation for the time evolution of the phases of a system of oscillators, equation (2.1), and can be used to model the synchronization of weakly coupled oscillators:

$$\dot{\theta}_i = \omega_i + \frac{K}{N} \sum_{j}^{N} \sin(\theta_j - \theta_i), \tag{2.1}$$

where $\dot{\theta}_i$ is the time derivative of the phase of the i-th oscillator; ω_i is the natural frequency of the i-th oscillator when it is not interacting with any other oscillator; N is the number of oscillators and K is a coupling constant. By introducing the complex order parameter $z(t)$ for the population of oscillators,

$$z(t) = r(t)e^{i\Psi(t)} = \frac{1}{N} \sum_{j=1}^{N} e^{i\theta_j(t)}, \tag{2.2}$$

with $r(t)$ quantifying the global oscillator coherence, and $\Psi(t)$ being the average phase, it is possible to look at equation (2.1) as a system of oscillators forced by a mean field $\Psi(t)$:

$$\dot{\theta}_i = \omega_i + r(t)K \sin(\Psi(t) - \theta_i). \tag{2.3}$$

The Kuramoto model has a mean-field steady state solution, found by Kuramoto in his original work, that first gave insight about this phenomena.

2.1 Mean-field continuous solution

It is possible to reach some analytical results by employing a mean-field continuous approach. Kuramoto was looking for steady state solutions, which in this context means that $r(t)$ is constant and that $\dot{\Psi} = \Omega$, with Ω being a constant frequency. It is then possible to look at the system in the reference frame rotating at Ω and setting $\Psi = 0$, as we can choose the reference frame as we wish without loss of generality. The equation (2.3) can be rewritten this way:

$$\begin{aligned}\dot{\theta}_i &= \omega_i' + r(t)K\sin(\Psi(t) - \theta_i) \\ &= \omega_i' - \Omega + rK\sin(0 - \theta_i) \\ &= \omega_i - rK\sin(\theta_i), for \quad i = 1, ..., N.\end{aligned} \tag{2.4}$$

With $\omega_i = \omega_i' - \Omega$. Due to the mean-field coupling we got N independent oscillators which can have 2 different long time behaviours: if $|\omega_i| < rK$ the oscillator will approach the fixed point

$$\sin(\theta_i) = \frac{|\omega_i|}{rK}, \tag{2.5}$$

and become 'locked', moving at the same frequency, Ω as our frame of reference; if $|\omega_i| > rK$ the oscillators phase will 'drift' without a fixed frequency, having a different frequency depending on its phase. This second behaviour at first glance does not seem to agree with our hypothesis of a steady state solution and was explained by Kuramoto by using a stationary distribution of oscillators' phases in a circle, $\rho(\omega, \theta)$, meaning that even though the oscillators would move non-uniformly the phase distribution of the ensemble would constant constant through time. This means we have 2 different populations, the 'locked', or synchronous population n_s and the 'drifting', or asynchronous population n_{as}. In the $N \to \infty$ limit we can talk about a stationary continuous distribution $\rho(\omega, \theta)$ with $\rho(\omega, \theta)d\theta$ being the fraction of oscillators with frequency ω that have phases between θ and $\theta + d\theta$. For this distribution to be stationary it has to be inversely proportional to the frequency, $\dot{\theta}$, at a given phase [27], due to the continuity equation $\frac{\partial \rho}{\partial t} = -\frac{\partial}{\partial \theta}(\rho\dot{\theta})$, meaning that there will be many oscillators with lower frequency and there will be few with high frequencies. It is important to distinguish the frequency of each oscillator, given by θ_i, and the intrinsic frequency of each oscillator, ω_i, which follows a distribution $g(\omega)$. The two different populations have different expressions for $\rho(\omega, \theta)$. The synchronous population, where all oscillators have an intrinsic frequency smaller that rK, has all oscillators in their fixed point given by equation 2.5, taking into account the normalization condition $\int_0^{2\pi} \rho(\omega, \theta)d\theta = 1$ for all ω, its possible to write the stationary distribution for the synchronous as:

$$\rho(\omega, \theta) = \delta(\theta - \sin^{-1}(\frac{\omega}{rK})). \tag{2.6}$$

We can then calculate $\rho(\omega, \theta)$ for asynchronous population using equation (2.4):

$$\rho(\omega, \theta) = \frac{C}{|\omega - rK\sin(\theta)|}, \tag{2.7}$$

with the normalization constant, C, being determined by the normalization condition $\int_0^{2\pi} \rho(\omega, \theta)d\theta = 1$ for all ω, yielding:

$$C = \frac{1}{2\pi}\sqrt{\omega^2 - (Kr)^2}.$$

From the initial assumption that the system is in a steady state we can infer that the population average of the order parameter is a constant, and remembering that we can set $\Psi = 0$, $\langle e^{i\theta} \rangle = \frac{1}{N}\sum_{j=0}^{n} e^{i\theta_j} = re^{i\psi} = r$, and we can split the population in the "drifting" and "locked" :

$$\begin{aligned}\langle e^{i\theta} \rangle &= \langle e^{i\theta} \rangle_{locked} + \langle e^{i\theta} \rangle_{drift}, \\ r &= \langle e^{i\theta} \rangle_{locked} + \langle e^{i\theta} \rangle_{drift},\end{aligned} \tag{2.8}$$

The contribution of the term $\langle e^{i\theta} \rangle_{drift}$ is 0:

$$\begin{aligned}\langle e^{i\theta}\rangle_{drift} &= \int_{|\omega|>Kr}\int_{-\pi}^{\pi} e^{i\theta} g(\omega)\rho(\omega,\theta)d\theta d\omega \\ &= \int_{|\omega|>Kr}\int_{0}^{\pi} e^{i\theta} g(\omega)\rho(\omega,\theta)d\theta d\omega + \int_{|\omega|>Kr}\int_{-\pi}^{0} e^{i\theta} g(\omega)\rho(\omega,\theta)d\theta d\omega\end{aligned}$$

Using the assumption that $g(\omega) = g(-\omega)$ and noting from equation (2.7) that $\rho(\omega,\theta) = \rho(-\omega,\theta+\pi)$

$$\begin{aligned}\langle e^{i\theta}\rangle_{drift} &= \int_{|\omega|>Kr}\int_{0}^{\pi} e^{i\theta} g(\omega)\rho(\omega,\theta)d\theta d\omega + \int_{|\omega|>Kr}\int_{-\pi}^{0} e^{i\theta} g(-\omega)\rho(-\omega,\theta+\pi)d\theta d\omega \\ &= \int_{|\omega|>Kr}\int_{0}^{\pi} e^{i\theta} g(\omega)\rho(\omega,\theta)d\theta d\omega + \int_{|\omega'|>Kr}\int_{0}^{\pi} e^{i\theta'-\pi} g(\omega')\rho(\omega',\theta')d\theta' d\omega' \\ &= \int_{|\omega|>Kr}\int_{0}^{\pi} e^{i\theta} g(\omega)\rho(\omega,\theta)d\theta d\omega - \int_{|\omega|>Kr}\int_{0}^{\pi} e^{i\theta} g(\omega)\rho(\omega,\theta)d\theta d\omega \\ &= 0\end{aligned}$$

The oscillators that are phase-locked will have approached the fixed point given by equation 2.5, with the phases of these oscillators being determined by the initial frequency distribution, $g(\omega)$. The contribution of the term $\langle e^{i\theta}\rangle_{locked}$ term can be split into its real and imaginary parts. The imaginary contribution is 0, by using $g(\omega) = g(-\omega)$:

$$\begin{aligned}\langle \sin(\theta)\rangle_{locked} &= \int_0^{2\pi}\int_{-Kr}^{Kr} \sin(\theta)\rho(\omega,\theta)g(\omega)d\omega d\theta \\ &= \int_0^{2\pi}\int_{-Kr}^{Kr} \sin(\theta)\delta(\theta - \sin^{-1}(\frac{\omega}{rK}))g(\omega)d\omega d\theta \\ &= \int_{-Kr}^{Kr} \frac{\omega}{Kr} g(\omega)d\omega \\ &= 0.\end{aligned}$$

The real contribution is equal to:

$$\begin{aligned}\langle \cos(\theta)\rangle_{locked} &= \int_0^{2\pi}\int_{-Kr}^{Kr} \cos(\theta)\rho(\omega,\theta)g(\omega)d\omega d\theta \\ &= \int_0^{2\pi}\int_{-Kr}^{Kr} \cos(\theta)\delta(\theta - \sin^{-1}(\frac{\omega}{rK}))g(\omega)d\omega d\theta\end{aligned}$$

By integrating in theta and then using equation 2.5 to write $\omega = \sin(\theta)Kr$ and $d\omega = \cos(\theta)Kr$:

$$\begin{aligned}\langle \cos(\theta)\rangle_{locked} &= \int_{-Kr}^{Kr} \cos(\sin^{-1}(\frac{\omega}{rK}))g(\omega)d\omega \\ &= Kr\int_{-\frac{\pi}{2}}^{\frac{\pi}{2}} \cos^2(\theta)g(Kr\sin(\theta))d\theta\end{aligned}$$

The self-consistency condition now is:

$$r = Kr\int_{-\frac{\pi}{2}}^{\frac{\pi}{2}} \cos^2(\theta)g(Kr\sin(\theta))d\theta \tag{2.9}$$

This condition has a trivial solution $r = 0$, which translates to all oscillators belonging to the asynchronous population and that $\rho(\omega,\theta) = \frac{1}{2\pi}$, meaning that they cover the circle homogeneously. There is a second branch of solution that arises from letting $r \to 0^+$:

$$\begin{aligned} 1 &= K_c \int_{-\frac{\pi}{2}}^{\frac{\pi}{2}} \cos^2(\theta) g(0^+) d\theta, \\ K_c &= \frac{1}{\int_{-\frac{\pi}{2}}^{\frac{\pi}{2}} \cos^2(\theta) g(0^+) d\theta}, \\ K_c &= \frac{2}{\pi g(0^+)}. \end{aligned} \tag{2.10}$$

The value K_c is the critical coupling strength above which some part of the oscillators spontaneously synchronize and the oscillators split into two populations, the synchronous and the asynchronous. The total population is given by the integral:

$$n_s + n_{as} = \int_0^{2\pi} \int_{-\infty}^{\infty} \rho(\omega,\theta) g(\omega) d\omega d\theta, \tag{2.11}$$

with $n_s + n_{as} = 1$. The steady state value for this populations depend on the initial frequency distribution $g(\omega)$ on K and on r_∞:

$$\begin{aligned} n_s &= \int_0^{2\pi} \int_{-Kr}^{Kr} \delta(\theta - \sin^{-1}(\frac{\omega}{rK})) g(\omega) d\omega d\theta, \\ n_{as} &= \int_0^{2\pi} \int_{|-\omega|>Kr} \frac{1}{2\pi} \frac{\sqrt{\omega^2 - (Kr)^2}}{|\omega - rK\sin(\theta)|} g(\omega) d\omega d\theta. \end{aligned} \tag{2.12}$$

Kuramoto calculated how r grows given a specific $g(\omega) = \frac{\gamma}{\pi(\gamma^2+\omega^2)}$, the Cauchy distribution, by solving equation (2.9):

$$r = \sqrt{1 - \frac{K_c}{K}}. \tag{2.13}$$

The $N \to \infty$ limit also allows us to make predictions about the time evolution of the order parameter [31].The state of the system at time t is given by distribution function, $f(\omega,\theta,t)$, which can be integrated to give the initial, time independent, phase distribution $g(\omega)$:

$$\int_0^{2\pi} f(\omega,\theta,t) d\theta = g(\omega), \tag{2.14}$$

It is then possible to write complex order parameter, $z = re^{i\Psi}$ using this distribution function:

$$z = \int_0^{2\pi} d\theta \int_{-\infty}^{+\infty} d\omega f e^{i\theta}, \tag{2.15}$$

and using the Euler's formula to rewrite $\frac{1}{N}\sum_j \sin[\theta_j - \theta_i]$ in the expression for $\dot{\theta}$, equation (. 2.1) it is possible to write it as:

$$\dot{\theta} = \omega + \frac{K}{2i}(ze^{-i\theta} - z^* e^{i\theta}) \tag{2.16}$$

distribution function, $f(\omega,\theta,t)$, obeys the continuity equation for the conservation of the number of oscillators, $\frac{\partial f}{\partial t} + \frac{\partial}{\partial \theta}\{\dot{\theta} f\} = 0$, and it is possible to write:

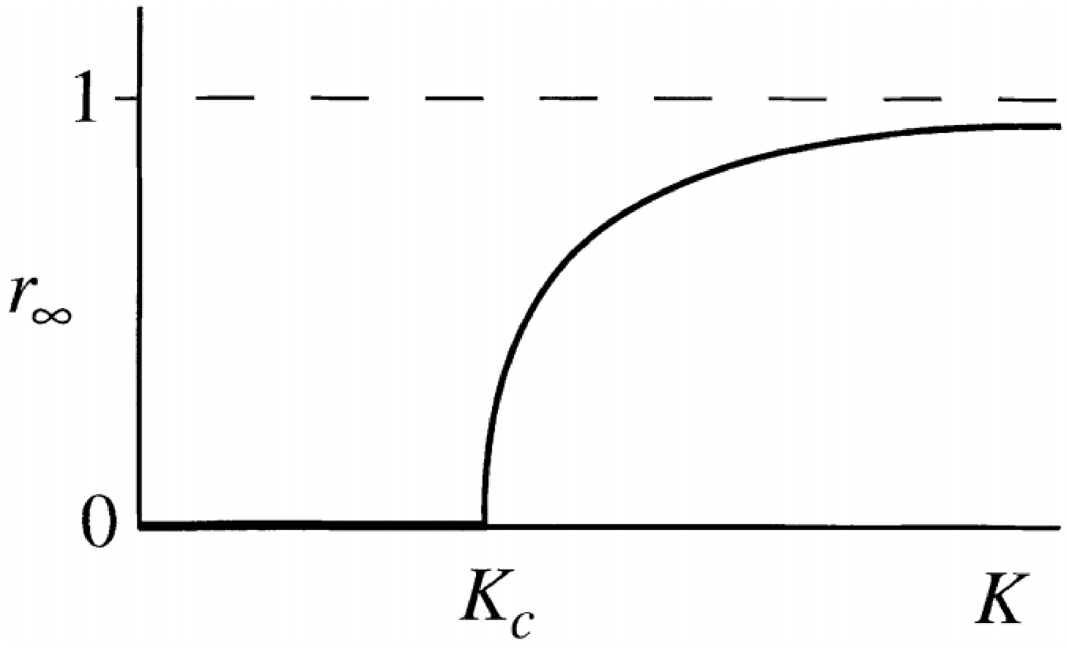

Figure 2.1: **Second order phase transition of the Kuramoto model.**For the Cauchy distribution of frequencies the Kuramoto model the order parameter is 0 below a critical value of K,K_C and above K_C, r behaves like $r = \sqrt{1 - \frac{K_c}{K}}$

$$\frac{\partial f}{\partial t} + \frac{\partial}{\partial \theta}\left\{\left[\omega + \frac{K}{2i}\left(ze^{-i\theta} - z^{*}e^{i\theta}\right)\right] f\right\} = 0 \tag{2.17}$$

can expand this distribution function in a Fourier series in θ:

$$f(\omega, \theta, t) = \frac{g(\omega)}{2\pi}\left\{1 + \sum_{n=1}^{\infty} f_n(\omega, t)e^{(in\theta)} + \sum_{n=1}^{\infty} f_n^{*}(\omega, t)e^{(-in\theta)}\right\}. \tag{2.18}$$

By using the anzat $f_n = \alpha^n$ used in [31], which is consistent with both the incoherent state, $f = \frac{g(\omega)}{2\pi}$ with $\alpha(t) = 0$ and also with the synchronized state with $|z| = r$, with r a constant, it is possible to write the continuity function, equation (. 2.17) in the following form:

$$\begin{gathered}\frac{\partial}{\partial t}\frac{g(\omega)}{2\pi}\left[1 + \sum_{n=1}^{\infty}\left(\alpha^{n}e^{in\theta} + \alpha^{*n}e^{-in\theta}\right)\right] + \\ \frac{\partial}{\partial \theta}\left\{\left[\omega + \frac{K}{2i}\left(ze^{-i\theta} - z^{*}e^{i\theta}\right)\right]\frac{g(\omega)}{2\pi}\left[1 + \sum_{n=1}^{\infty}\left(\alpha^{n}e^{in\theta} + \alpha^{*n}e^{-in\theta}\right)\right]\right\} = 0,\end{gathered} \tag{2.19}$$

which can be written as:

$$
\begin{aligned}
&\sum_{n=1}^{\infty}\left(n\dot{\alpha}\alpha^{n-1}e^{in\theta}+n\dot{\alpha}^{*}\alpha^{*n-1}e^{-in\theta}\right)\frac{g(\omega)}{2\pi}-ziG(\omega)e^{-i\theta}-z^{*}iG(\omega)e^{i\theta}\\
&+G(w)zi\sum_{n}^{\infty}\alpha^{n}(n-1)e^{i\theta(n-1)}-G(w)z^{*}i\sum_{n}^{\infty}a^{n}(n+1)e^{i\theta(n+1)}+\Omega(w)\sum_{n=1}^{n}in\alpha^{n}e^{in\theta}\\
&-G(w)zi\sum\alpha^{*n}(n+1)e^{-i\theta(n+1)}+G(\omega)z^{*}i\sum\alpha^{*n}(n-1)e^{-i\theta(n-1)}-\Omega(\omega)\sum_{n=1}^{n}in\alpha^{*n}e^{-in\theta}=0,
\end{aligned}
\tag{2.20}
$$

with $G(\omega)=\frac{kg(\omega)}{4i\pi}$ and $\Omega=\frac{\omega g(\omega)}{2\pi}$ and $\dot{\alpha}=\frac{d\alpha}{dt}$. This equation has to be valid for any value of θ so we know that for this equality to hold we have to look at the powers of $e^{i\theta}$. The first power and all higher order give us an expression for the time evolution of α:

$$
\frac{\partial\alpha}{\partial t}+(\frac{K}{2})\left(z\alpha^{2}-z^{*}\right)+i\omega\alpha=0. \tag{2.21}
$$

Substituting the Fourier expansion eq. (2.18) in the definition complex order parameter, z, eq. (2.15) we can get a relation between z and α:

$$
z=\int_{-\infty}^{+\infty}d\omega\alpha^{*}(\omega,t)g(\omega) \tag{2.22}
$$

This equation can be solved for the standard Cauchy distribution, $g(\omega)=\frac{1}{\pi(1+\omega^{2})}$ yielding $z=a^{*}(-i,t)$ and for the Dirac distribution, $g(\omega)=\delta(\omega-\omega_{D})$, yielding $z=a^{*}(\omega_{D},t)$. Because we will be looking at the Dirac distribution further in our work we will look with more detail in the case that expand $\omega_{D}=0$ case, although analytic solutions can be reached for other distributions. Writing the complex order parameter as $z=re^{i\Psi}$ and substituting α by z in equation (2.21) we can reach an expression for the time evolution of r:

$$
\frac{dr}{dt}=\frac{K}{2}\left(r-r^{3}\right) \tag{2.23}
$$

,

that can be solved for a given initial condition $r(0)$ as :

$$
r(t)=\frac{1}{\sqrt{1+e^{-K(t-t_{0})}}}, \tag{2.24}
$$

with

$$
t_{0}=\frac{\ln(\frac{1}{r(0)^{2}}-1)}{K}. \tag{2.25}
$$

The curve given by $r(t)$ is the square root of the logistic curve and their shapes resemble one another. K, the coupling parameter, governs how fast the curve reaches its saturation value, 1, and t_0 is related to the horizontal shift of the curve, being inversely proportional to K. To see how widely the Kuramoto model can be applied we will give examples of its uses in control theory and also in neurobiology.

2.2 Examples

It is also possible to use the Kuramoto model in control theory, more specifically in motor coordination [32]:

$$
\begin{aligned}
\dot{r}_i &= v_p e^{i\theta_i(t)}, \\
\dot{\theta}_i &= \omega_i + \frac{K}{N_i}\sum_{i,j}\sin(\theta_j - \theta_i),
\end{aligned}
\tag{2.26}
$$

with v_p being the propulsion velocity of the steering agents, θ_i representing the heading direction and ω the steering velocity of each agent, with K being the coupling between the different heading directions.

By changing some parameters of how thesesteering agents interact with their neighbours they can have different steering behaviours,see figure 2.2. By controlling their intrinsic frequencies ω_i and their coupling strength it is possible to display various flocking patterns, as seen in [33] and as shown by Vicsek [34], works that that demonstrated that thesesimple model can capture behaviour from animals, by simplifying them to these steering agents.

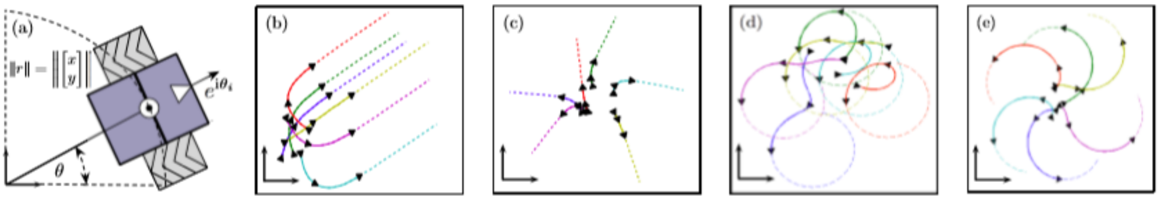
(a)
$\|r\| = \left\|\begin{bmatrix} x \\ y \end{bmatrix}\right\|$
$e^{i\theta_i}$
θ
(b)
(c)
(d)
(e)

Figure 2.2: **Application of the Kuramoto model in steering agents.** Panel (a) illustrates the particle kinematics (6). Panels (b)-(e) illustrate the controlled dynamics, eq. (2.26) with n=6 particles, a complete interaction graph, and identical and constant natural frequencies: ω_i(t) = 0 for all agents in panels (b) and (c) and ω_i(t) = 1 for all agents in panels (d) and (e). The values of K are $K = 1$ in panel (b) and (d) and K=1 in panel (c) and (e). The arrows depict the orientation, the dashed curves show the long-term position dynamics, and the solid curves show the initial transient position dynamics. As illustrated, the resulting motion displays "synchronized" or "balanced" heading angles for $K = 1$, and translational motion for ω_i(t) = 0, respectively circular motion for ω_i(t) = 1. Taken with permission from [1].

The Kuramoto model can also be used as an easy-to-solve model for neurons, as some of the behaviour it exhibits is qualitatively similar to synchronization behaviours found in neurons [2]. When considering Rulkov neurons [35], which is a model hard to solve analytically, the order parameter, that is defined similarly to eq. (4.3), behaves like the Kuramoto model, which is a easy to solve model numerically. Figure 2.3 shows how both models behave similarly, for both uniform and Cauchy distributions for the intrinsic frequencies and also for different oscillator couplings, all-to-all coupling or global coupling, Erdös–Rényi networks [36], small-world [37] and scale-free networks [38]. In the next section we will look into the main results of Brownian motion as a precursor to the modeling of our oscillators as a mixture of Brownian particles.

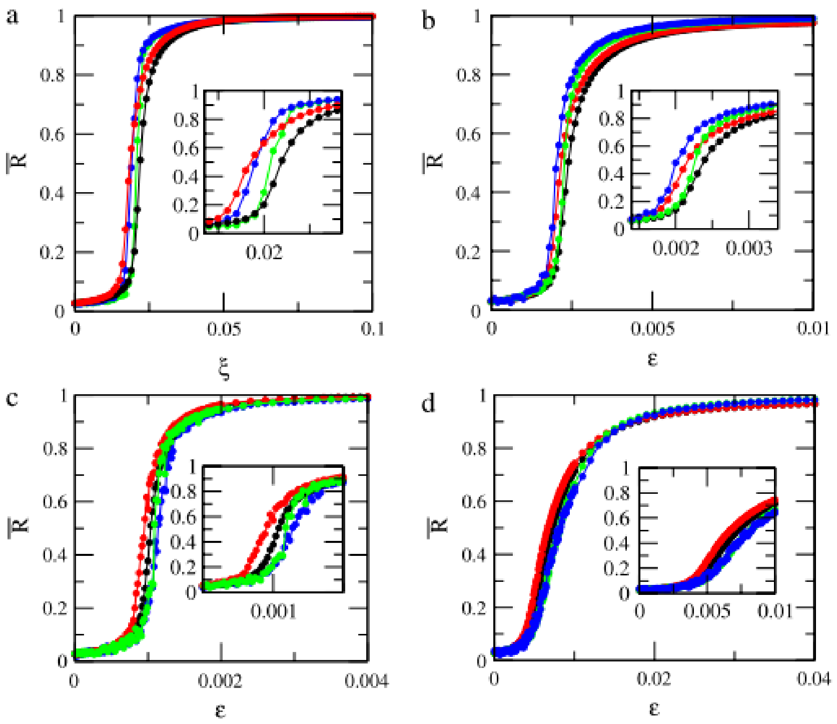

Figure 2.3: **Application of the Kuramoto model in networks of neurons.**Order parameter magnitude as a function of the coupling strength for a network of Rulkov neurons (black: uniform, red: Cauchy) and Kuramoto oscillators (green: uniform, blue: Cauchy) with N = 1000 nodes, for (a) global coupling, (b) Erdös–Rényi; (c) small-world, and (d) scale-free. Taken with permission from [2]

2.3 Simulations

To understand the Kuramoto model, we integrated the Kuramoto equation (2.1) using the Euler method and we calculated $r(t)$ given by equation (2.2) for different numbers of oscillators, N ranging from 10 to 1000, for different values of K, ranging from 0 to 2, and different distributions, $g(\omega)$, of ω_i, the Dirac distribution, $\delta(\omega)$, and the standard Cauchy distribution.

The behaviour of the order parameter, r, can be divided into two categories, it either goes to 0, as in figure 2.4(a-c), meaning that the system is not synchronized, or it increases and stabilizes at a specific value greater than 0, as observed in figure 2.4(d-f), which we denominate r_∞, and the closer the value of r_∞ is to 1 the more synchronized the system is.

We observed that this transition was mainly governed by the value of K, meaning that for the same value of N and the same ω_i distributions, systems would not synchronize below a critical point, K_C. This is the same behaviour predicted by Kuramoto where a second degree phase transition happens at the critical point K_C. The distribution of ω_i, $g(\omega)$, is also important as it determines the value of K_C and determines the value of r_∞ for K above K_C.

For values of K below the critical point K_C each oscillator phase drifts around the unit circle with an angular frequency that varies in time,as figure 2.5(a-b) shows, while for values of K greater than K_C a percentage of the oscillators become enthralled by a new common frequency with the phase difference between these oscillators becoming constant, meaning that they are synchronized,like in figure 2.5(c-d).

The time evolution of r can be obtained for some $g(\omega)$, like the Cauchy and the Dirac distributions, by solving equation (2.21) and equation (2.22), and it can be written as:

$$r(t) = \frac{r_\infty}{\sqrt{1 + e^{-\kappa(t-t_0)}}}, \tag{2.27}$$

with r_∞ being the value that $r(t)$ approaches at long times, κ being the growth rate and t_0 being a time shift related to the initial conditions, $t_0 = \frac{\ln(\frac{1}{r(0)^2}-1)}{K}$, with $r(0)$ being the initial condition. If we plot the value of r_∞ around the critical coupling K_C, calculated for the case the standard Cauchy distribution of ω_i, as figure 2.6(a) shows, it is possible to observe the behaviour described by Kuramoto, see figure 2.1. We observe that the stable solution for the steady state, $r_\infty = 0$, below K_C splits at K_C into a stable branch where r_∞ approaches 1 and a unstable branch where $r_\infty = 0$, which cannot be observed in simulations. The stable branch can be described by equation (2.13) and the results of our simulations match the predicted behaviour. For the case of the Dirac distribution of intrinsic frequencies we find that the value of r_∞ discontinuously jumps to one, as the only theoretical values allowed for this distribution are 0, for $K < K_C$, or 1, for $K > K_C$, this being called a first order phase transition, like in figure 2.6(b).

By plotting the value of the growth rate, κ, against K its we confirmed their equality, as predicted by equation (2.24), figure 2.7(a). We also observe that $t_0 \sim \frac{1}{K}$, the behaviour described by equation (2.25), like figure 2.7(b) shows. The value of κ and t_0 was calculated by fitting equation (2.27) to the simulation results of a specific system.

To study oscillators in networks with nodes which change their neighbours as if they were Brownian particles moving in space we firstly have to study Brownian motion.

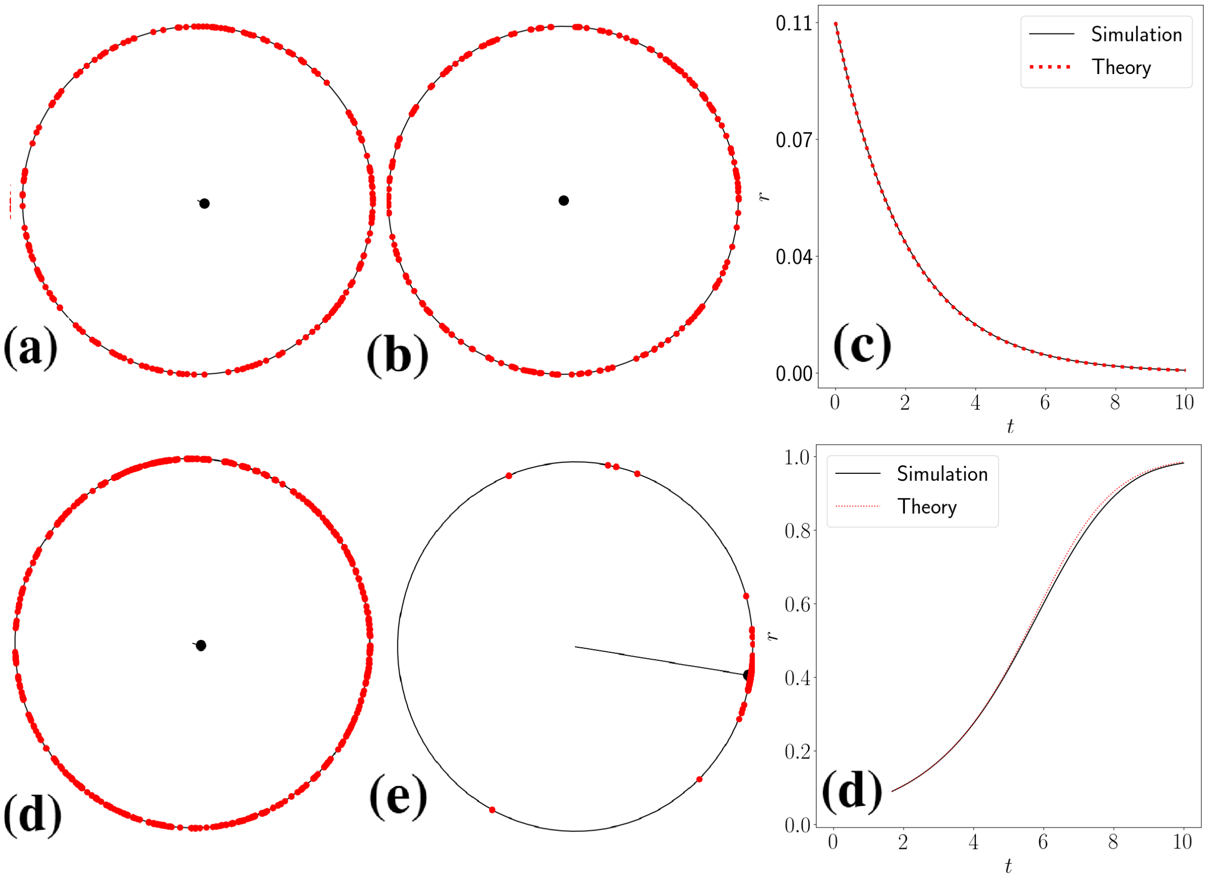

Figure 2.4: **Evolution of the order parameter.** Panels (a),(b),(d),(e) represent system of oscillators at a given time. The position of each red point in the unit circle is given by the phase of a specific oscillator and the position of the black point is given by the complex order parameter $re^{i\Psi(t)}$, equation 2.2. (a) and (d) show the initial configuration of the system with N = 500, and $g(\omega_i)$ the Dirac distribution, $\delta(\omega)$. The initial phases were drawn from an uniform distribution in the interval [0;2π]. The value of K is -1 and 1 respectively. (b) and (e) are the systems in (a) and (d) after 10000 timesteps, (c) and (f) corresponds to the time evolution of the value of r, the order parameter. The time evolution for this distribution can be solved analytically and is given by equation (2.24), which is represented as the dashed red line in the plot. In (c) the system remains not synchronized, $r \sim 0$, even after long time periods because the value of K is smaller than the critical value that allows for synchronization, which for this system is $K_C = 0$ In (f) the system synchronizes,$r \sim 1$, and remains phase-locked because the value of K is higher than the critical value of for synchronization, $K_C = 0$, for this system.

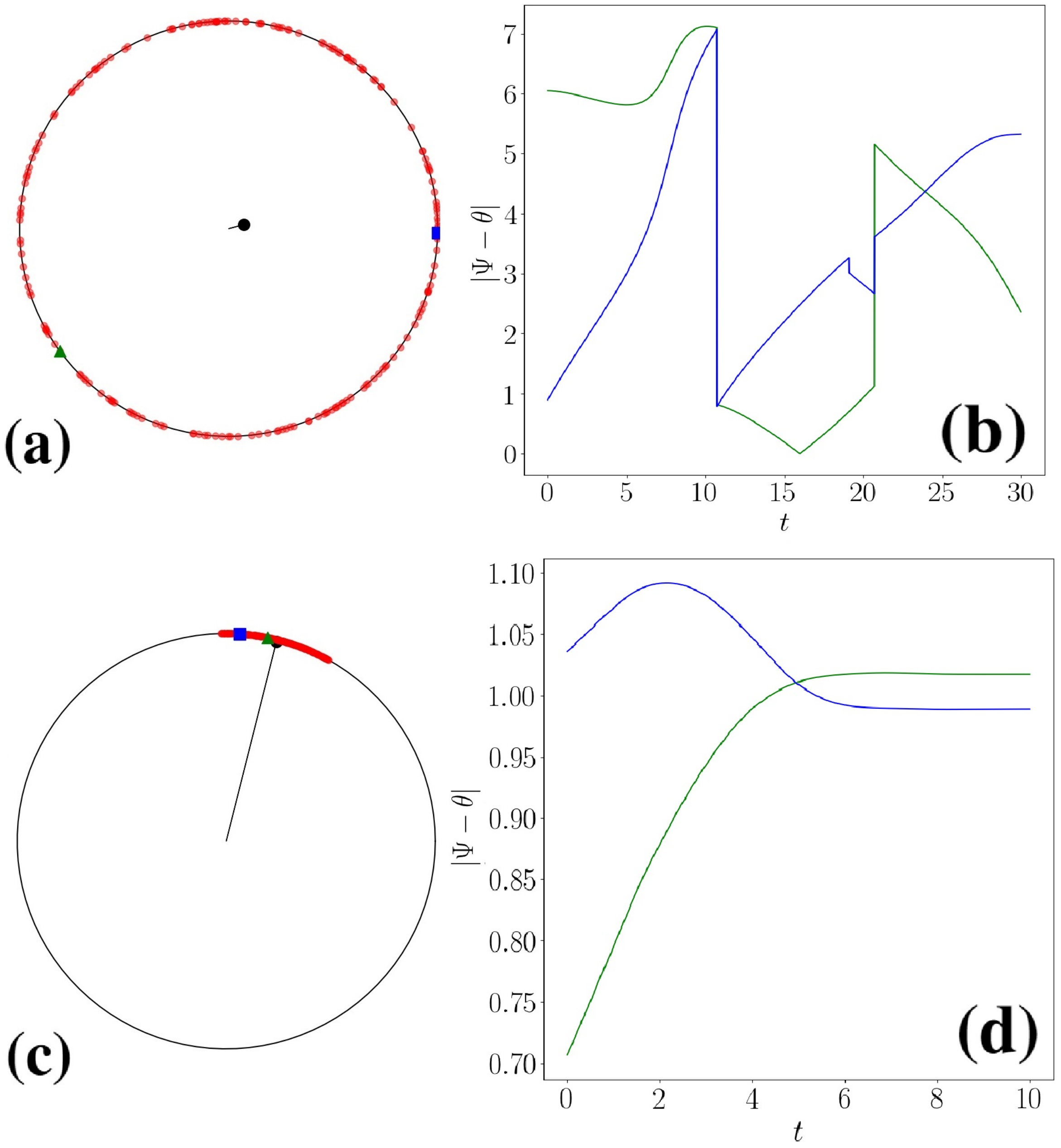

Figure 2.5: **Phase drifting and phase locking.** (a) and (c) shows the final configuration of a system of 200 oscillators, with a standard Cauchy distribution of frequencies after 50000 and 10000 timesteps respectively. The values of K were 1 for (a) and 3 for (b) The initial phases were drawn from an uniform distribution in the interval [0;2π]. The position of each red point in the unit circle is given by the phase of a specific oscillator and the position of the black point is given by the complex order parameter $re^{i\Psi(t)}$, equation 2.2. The green triangle and the blue square represent 2 oscillators chosen at random. (b) and (d) show the evolution of the difference of the chosen oscillators phase and $\Psi(t)$ in their respective colors. In (b) it is possible to observe the phase drift of the randomly chosen oscillators as their phase changes non uniformly. This system is does not synchronize because the value of K is below its critical value for synchronization, $K_C = 2$. In (d) we observe the phase-locking that is a characteristic of synchronization, with the phase difference of each oscillator staying constant in time. Synchronization is possible because value of K is larger than the critical value for synchronization, $K_C = 2$

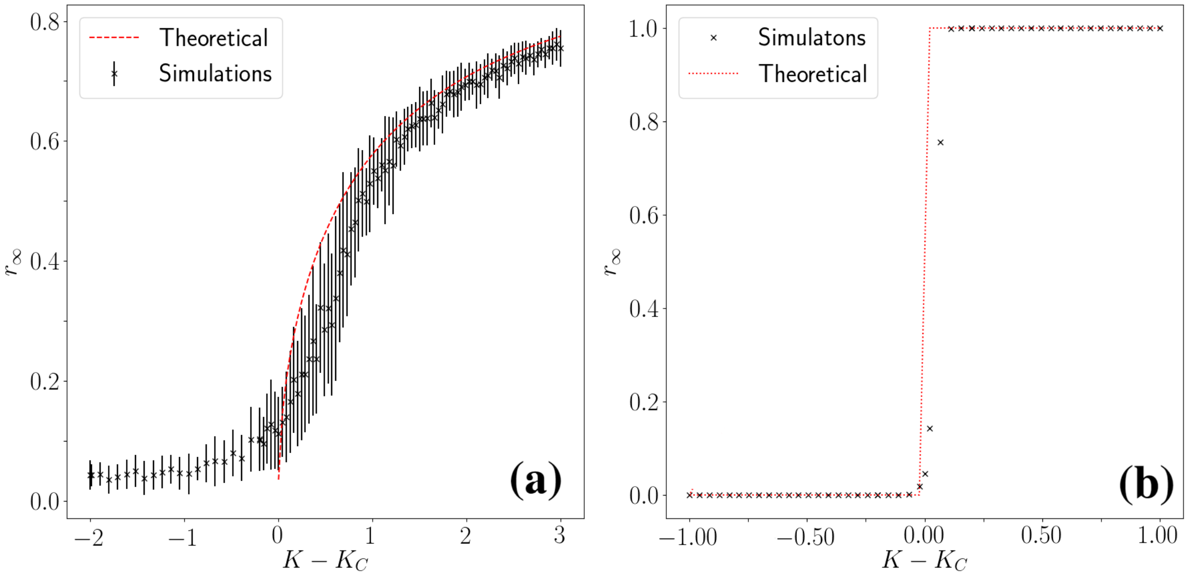

Figure 2.6: **Synchronization phase transition.** The nature of the Kuramoto phase transition depends on the distribution of the frequency distribution of its oscillators and also on the geometry. For the standard Cauchy distribution this transition is a second order phase transition. Below K_C the only stable steady state solution is $r = 0$, but above K_C this solution becomes unstable and the stable steady state solution becomes $r = \sqrt{1 - \frac{K_C}{K}}$ as shown in panel (a). The simulations are done for N = 500, the value of r_∞ of does not exactly match up with the theoretical behaviour for $N \to \infty$. Panel (b) shows the first order phase transition characteristic of the Dirac distribution for the oscillators frequency. The simulations are done for N = 500 and the values close to the critical point do not correspond to the theoretical results due to the long simulation times needed for the system to reach its stationary value.

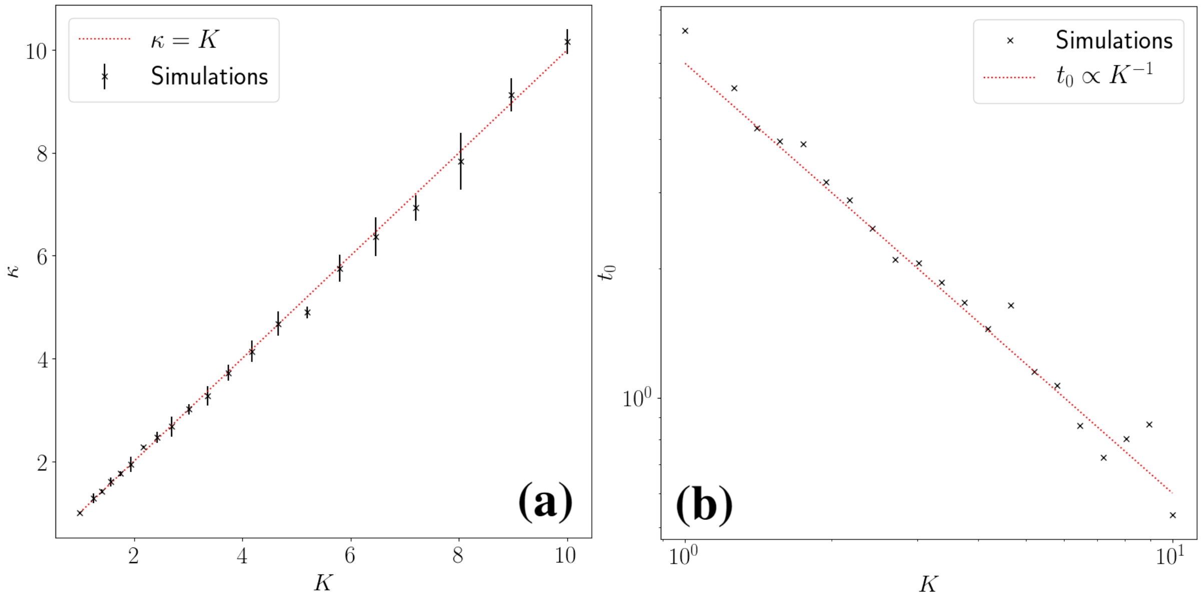

Figure 2.7: **Dependence of the r(t) curve parameters on K.** The value of the growth rate, κ, is equal to the value of K for the Dirac distribution of frequencies, $g(\omega) = \delta(\omega)$. The simulations match up with the theoretical result as we can observe in panel (a). The value of the timesift, t_0, is inversely proportional to the value of K for the Dirac distribution of frequencies, $g(\omega) = \delta(\omega)$.The simulations match up with the theoretical result as can be observed in panel (b). All the simulations were done with $N = 300$

Chapter 3

Brownian Motion

The random movement of small particles (μm) in fluids has been observed at least as far as 1784, by J. Ingen-Housz [39], who described the irregular motion of coal particles immersed in a fluid, but the name for this kind of motion, Brownian motion, is associated with Robert Brown [40], who in 1828 observed it in small pollen grains and other granular material immersed in water. The motion of these particles in a fluid is due to the interactions of the particles with the molecules of the fluid, which move randomly due to thermal fluctuations. The theoretical background for these phemomena was developed by Einstein [41] and Smoluchowski [42] with a probabilistic approach. This was later reformulated by Langevin [43] with stochastic differential equations, and Perin was awarded the Nobel Prize by confirming some theoretical claims with the experimental observation of this motion [44].

3.1 Analytic Results

At a mesoscopic timescale, larger than the duration of the interaction of a fluid molecule with a Brownian particle, the motion of a Brownian particle can be modeled by the Langevin equation:

$$m\dot{\vec{v}} = -\nabla U(\vec{r}) - \gamma\vec{v} + \vec{F_r}, \tag{3.1}$$

where m is the mass of the particle; $\vec{r}$ is the position of the particle; $U(\vec{r})$ is the external potential; γ is the friction constant that models the interaction of the particle with the fluid environment; $\vec{v}$ is the velocity of the particle; and $\vec{F_r}$ is a random force applied to the particle accounting for the random kicks of the fluid molecules on the particle surface. The random force $\vec{F_r}$ has the following properties [45]:

- it is, for a uniform system, independent of the particle position;
- its average over time (or over different realizations) is 0, $\langle\vec{F_r}\rangle = 0$;
- it is uncorrelated in timescales larger than the duration of one molecule kick, $\langle F_r\vec{(t_1)}F_r\vec{(t_2)}\rangle = 2A\delta(t_1 - t_2)$. A is given by the equation $A = \gamma k_b T$, where γ is the friction constant in equation (3.1); k_b is the Boltzmann constant; and T is the temperature of the fluid.
- In numerical simulations, this force is chosen to be Gaussian distributed, with mean 0 and standard deviation $2\gamma k_b T$.

If we consider the case of a free, $U(x) = 0$, Brownian particle moving in one dimension, the solution to equation (3.1) with initial condition $v(t=0) = v_0$ is:

$$v(t) = v_0 e^{-\frac{\gamma t}{m}} + e^{-\frac{\gamma t}{m}} \int_0^t e^{\frac{\gamma t'}{m}} \frac{F_r(t')}{m} dt' \tag{3.2}$$

The average velocity of the particle decays exponentially:

$$\begin{aligned} \langle v(t) \rangle &= \langle v_0 e^{-\frac{\gamma t}{m}} \rangle + e^{-\frac{\gamma t}{m}} \int_0^t e^{\frac{\gamma t'}{m}} \frac{\langle F_r(t') \rangle}{m} dt', \\ \langle v(t) \rangle &= v_0 e^{-\frac{\gamma t}{m}}, \end{aligned} \tag{3.3}$$

due to the fact that $\langle F_r \rangle = 0$. We can then say that for times much larger than the relaxation time $\frac{m}{\gamma}$ the particle has no drift velocity and we can consider $\langle v(t) \rangle = 0$. The mean-square velocity is:

$$\begin{aligned} \langle v^2(t) \rangle &= v_0^2 e^{-\frac{2\gamma t}{m}} + \frac{e^{-\frac{2\gamma t}{m}}}{m^2} \int_0^t \int_0^t e^{\frac{\gamma(t'+t'')}{m}} \langle F_r(t') F_r(t'') \rangle dt' dt'', \\ &= v_0^2 e^{-\frac{2\gamma t}{m}} + \frac{e^{-\frac{2\gamma t}{m}}}{m^2} \int_0^t \int_0^t e^{\frac{\gamma(t'+t'')}{m}} \gamma k_b T \delta(t' - t'') dt' dt'', \\ &= v_0^2 e^{-\frac{2\gamma t}{m}} + \frac{k_b T}{2m} (1 - e^{-2\frac{\gamma}{m} t}), \end{aligned} \tag{3.4}$$

which is the the result agrees with the equipartition theorem for the long time limit as $\langle v^2(t \to \infty) \rangle = \frac{k_b T}{2m}$. Integrating equation (3.2), with initial condition $x(t=0) = x_0$, it is possible to calculate the particle displacement:

$$x(t) = x_0 + \frac{m}{\gamma} v_0 (1 - e^{-\frac{\gamma t}{m}}) + \int_0^t \int_0^{t'} e^{-\frac{\gamma(t'-t'')}{m}} F_r(t'') dt'' dt' \tag{3.5}$$

in such a way that the average displacement is given by $\langle x(t) \rangle = x_0 + \frac{m}{\gamma} \vec{v_0} (1 - e^{-\frac{\gamma t}{m}})$. We can obtain the mean square displacement by calculating $\langle [\vec{r}(t) - \vec{r}(t')]^2 \rangle$:

$$\langle [x(t) - x(t')]^2 \rangle = (v_0^2 m^2 - k_b T) \frac{(e^{-\frac{\gamma t'}{m}} - e^{-\frac{\gamma t}{m}})^2}{\gamma^2} + \frac{2 k_b T}{\gamma} [|t - t'| - \frac{1 - e^{\frac{-\gamma |t - t'|}{m}}}{\gamma}] \tag{3.6}$$

If we look at this expression for values of t and t' smaller than the relaxation time $\frac{m}{\gamma}$ we see that the particle moves balistically with its initial velocity, and that for values much larger than the relaxation time averaging over the initial velocities and setting $t' = 0$ yields:

$$\begin{aligned} \langle [x(t) - x(0)]^2 \rangle &= \frac{2 k_b T}{\gamma} |t| \\ &= 2D|t| \end{aligned} \tag{3.7}$$

which is called the Einstein relation. This relation couples the self diffusion coefficient,D, with the friction constant, γ. We will now look to some examples of applications of the Brownian dynamics.

3.2 Examples

It is possible to use Brownian dynamics to study real systems and make predictions about molecules or small particles (μm), like in [3] where the self assembly of amphiphiles into vesicles is studied by using equation (3.1) and an effective potential U to mimic the hydrophobic and hydrophobic behaviour of amphiphilic molecules:

$$\begin{aligned} m\ddot{\vec{r_{i,j}}} &= -\nabla_r U - \gamma \vec{v_{i,j}} + \vec{F^r_{i,j}} \\ U &= \sum_{i \neq i'} U_{\text{rep}}\left(\left|\mathbf{r}_{i,j} - \mathbf{r}_{i',j'}\right|\right) + \sum_{j=2,3} U_{\text{hp}}\left(\rho_{i,j}\right) \\ \frac{U_{\text{rep}}(r)}{\epsilon} &= e^{-20(r/\sigma - 1)} \\ \frac{U_{hp}(\rho)}{\epsilon} &= \begin{cases} -0.5\rho & \rho < \rho^* - 1 \\ 0.25(\rho - \rho^*)^2 - c & \rho^* - 1 < \rho < \rho^* \\ -c & \rho > \rho^* \end{cases} \\ \rho_{i,j} &= \sum_{i \neq i', j'=2,3} h\left(\left|\mathbf{r}_{i,j} - \mathbf{r}_{i'}, j'\right|\right), \\ h(r) &= \frac{1}{\exp\{20(r/\sigma - 1.9)\} + 1} \end{aligned} \tag{3.8}$$

where i corresponds to the index of the amphiphilic molecule and j corresponds to the index of constituent particles that make it up, $j = 1$ is the hydrophilic one and $j = 2, 3$ the hydrophobic ones, σ is the soft radius of each particle, $\rho i, j$ is the number of hydrophobic particles in the sphere whose radius is approximately 1.9σ. The function $h(r)$ is cut at 1.6σ and 2.2σ: $h(r) = 1$ at $r < 1.6\sigma$ and $h(r) = 0$ at $r > 2.2\sigma$. and c and ρ^* are empirical parameters. The hydrophobic interaction is mimicked by U_{hp}, at low density ($\rho < \rho^* - 1$), U_{hp} works as the pair-wise potential $h(r)$. It is assumed that the particle is shielded by hydrophobic particles from solvent molecules and hydrophilic particles at ρ^*. Thus, U_{hp} is constant at higher density ($\rho > \rho^*$). In [3] they demonstrate how this simple model can create bi-layer structures like the vesicles, figure 3.1 found in organism cells, showing that it is possible to form complex structures of particles that move randomly by choosing with the a specific inter-particle interaction.

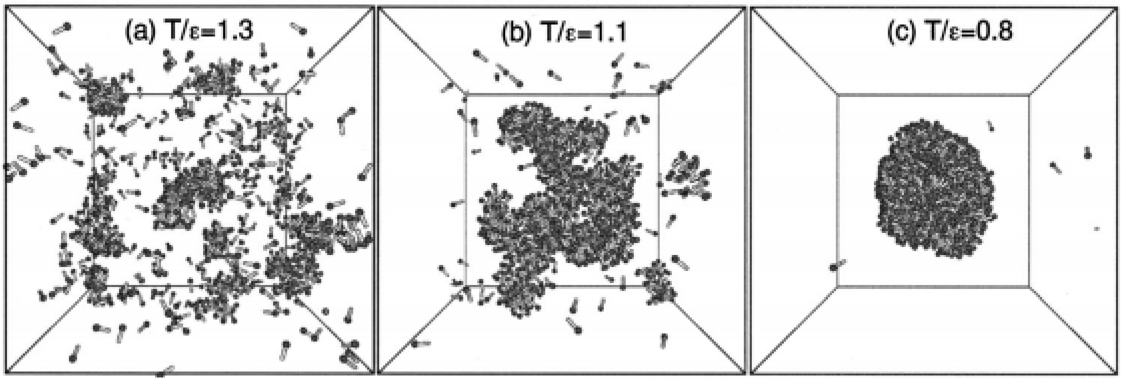

Figure 3.1: **Formation of micels by anphiphilic molecules.** By varying the ration between the temperature, T and the strength of the hydrophilic interaction, ϵ it is possible to control the formation of vesicles. Figure taken with permission from [3].

It is also possible to create Brownian particles in laboratory and use them as probes of microscopic

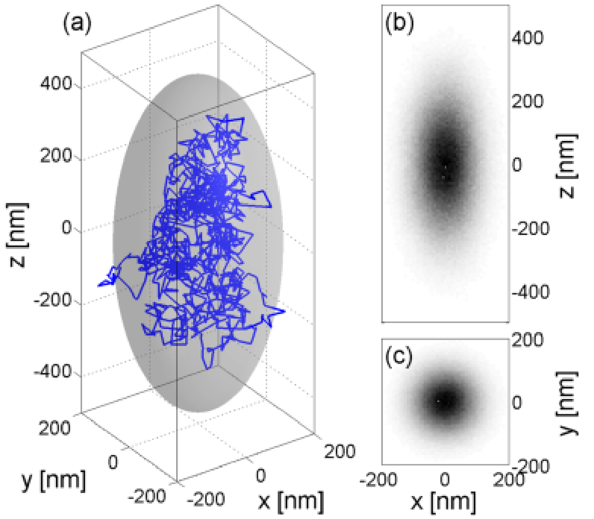

Figure 3.2: **Brownian particle in an optical trap**. (a) Trajectory of a Brownian particle in an optical trap. The particle explores an ellipsoidal volume around the center of the trap, as evidenced by the shaded area which represents an equiprobability surface. (b) and (c) The probability distributions of finding the particle in the z- and y-planes follow a twodimensional Gaussian distribution around the trap center. Taken with permission from [4].

forces [4]. Understanding the dynamics of Brownian particles inside an optical trap is essential to make nanoscale force measurements as discussed in [4]. After comparing their numerical results to results that can be calculated analytically they can make numerical predictions for particles trapped in optical traps, see figure 3.2.

3.3 Simulations

To explore some of the results given by the theory of Brownian motion and as a preparation to our modeling of a binary mixture of Brownian oscillators we used LAMMPS[46], Large-scale Atomic/Molecular Massively Parallel Simulator, which is a C++ library optimized to do molecular dynamics. To validate our LAMMPS script we used it to simulate a system that consisted of a single particle moving in 2 dimensions, in a box with dimensions $L \times L$, with periodic boundary conditions. LAMMPS applies a Langevin thermostat as described in [47] modeling a background implicit solvent and performs constant NVE integration, where N stands for the number of particles, V for volume and E for energy,[48]. LAMMPS integrates these equations of motion using the Verlet method:

$$\begin{aligned} m\ddot{\vec{r_i}} &= -\nabla U(\vec{r_i}) + \vec{F_f^i} + \vec{F_r^i}, \\ U(\vec{r_i}) &= \begin{cases} \sum_j 4\epsilon[(\frac{\sigma}{r_{ij}})^{12} - (\frac{\sigma}{r_{ij}})^{6}], |\vec{r_i} - \vec{r_j}| < \sqrt[6]{2}, \\ 0, r_{ij} > \sqrt[6]{2}. \end{cases} \\ \vec{F_f^i} &= -\frac{m}{damp}\vec{v}, \\ \vec{F_r^i} &\propto \sqrt{\frac{k_B T m}{dt * damp}} \end{aligned} \tag{3.9}$$

where the index i indicates the index of the particle, the position of the particle,$U(\vec{r_i})$ is the Lennard-Jones potential, with ϵ being the depth of the potential and σ, diameter of a particle, is the viscous drag term that is proportional to the particle velocity $\vec{v}$, $\frac{m}{damp}$ taking the place of the friction constant, with m being the mass of the particle and $damp$ being a constant inversely related to the viscosity of the solvent. $\vec{F_r^i}$ is the random force that the particle feels due to the solvent atoms and $dt = 0.01$ being the simulation timestep. We use Leonard-Jones units, where the fundamental quantities m, mass of a particle, σ, ϵ and k_b are all equal to 1, and we use the following conversions from our dimensionless variables t^*, r^*, T^* values to the dimensional ones:

$$t = t^* \sqrt{\frac{m\sigma^2}{\epsilon}}, \tag{3.10}$$

$$r = r^* \sigma, \tag{3.11}$$

$$T = T^* \frac{\epsilon}{K_b}, \tag{3.12}$$

A Brownian particles explores 2D space without memory of its past, as figure 3.4(a) shows, with a trajectory that is random. As predicted by equation 3.7 the mean square displacement is related to temperature, T^*, and with the friction constant, γ, which in our case is related with the value of $damp$, and by setting T^* and $damp$ equal to 1 we get that the diffusion constant, D = 1, which is confirmed by the results of the simulations reported in figure 3.4(b). By plotting the mean square displacement (MSD) at different temperatures and constant $damp$, figure 3.4(c) and plotting the MSD at different $damp$ and constant temperatures, as in figure 3.4(d) we reproduce the Einstein relation, equation (3.7). As we wanted to simulate more than one oscillator we then explored what happens when we add more particles, increasing the density of the system,η defined as $\eta = \frac{N*\pi*\sigma^2}{4*L*L}$. The diffusion constant goes down as the systems packing fraction, η, goes up, figure 3.3, due to the steric interaction between the particles.

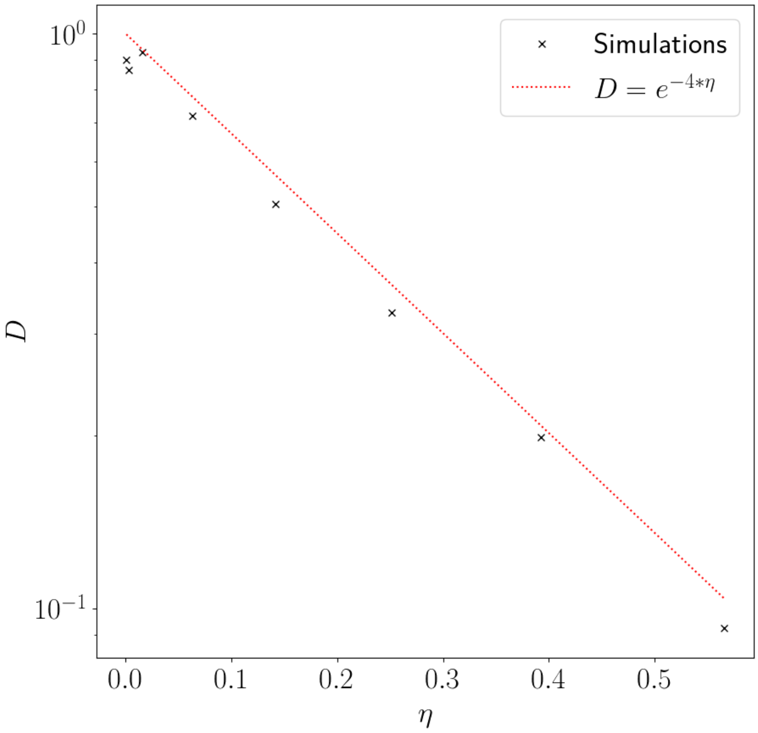

Figure 3.3: **Dependence of the diffusion constant with packing fraction.** As the packing fraction increases, and due to the steric interaction between particles, their mobility decreases and that is captured by the decrease of the diffusion constant measured in the system.

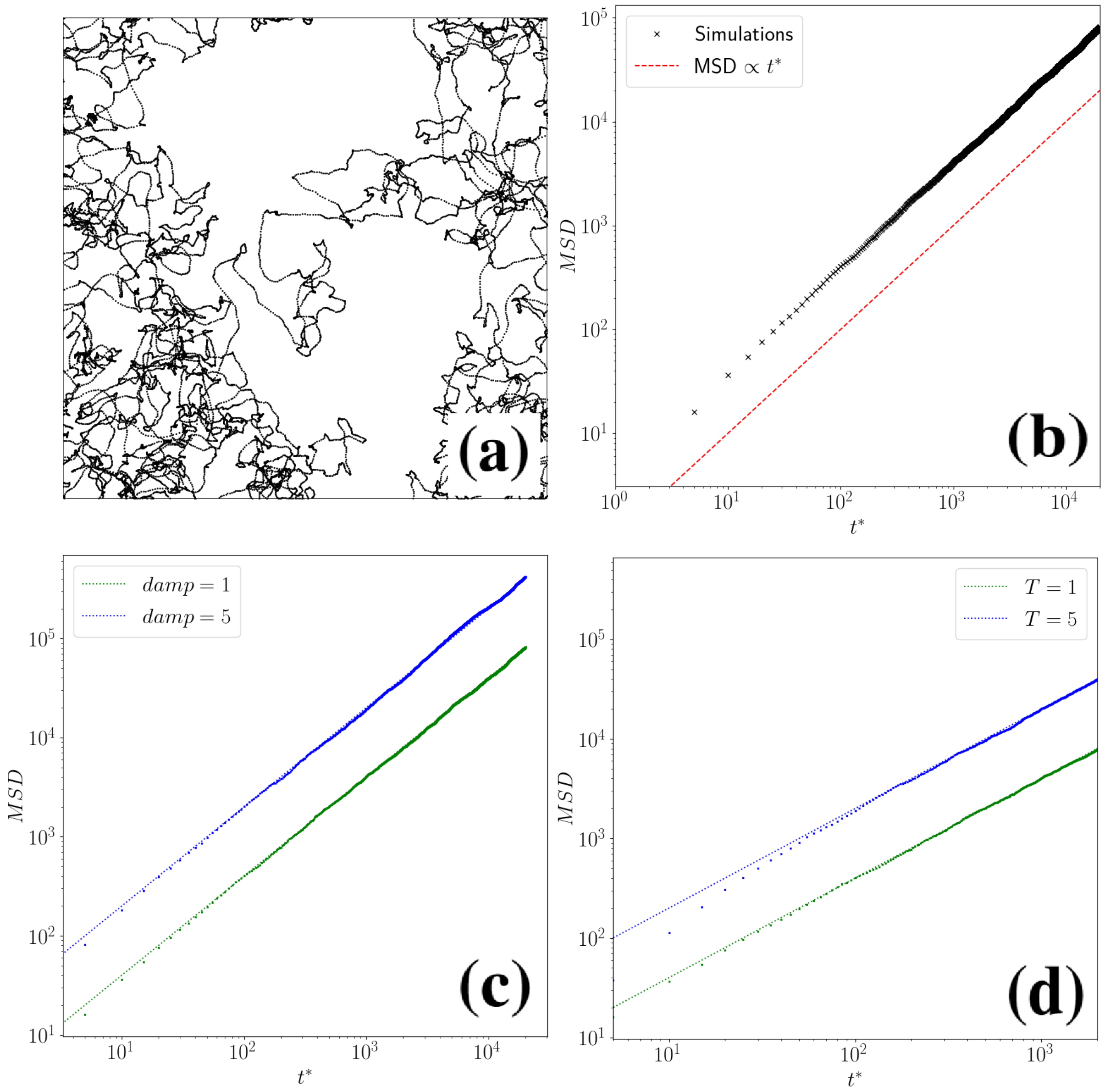

Figure 3.4: **Proprieties of a Brownian particle.** In panel (a) we can see the trajectories of a Brownian particle moving in a 50x50 box with periodic conditions. As can be observed the trajectory seems random and with no discernible pattern while exploring space. It is not possible to know the initial condition just by looking into the trajectory, as the system has no memory. In panel (B) the mean square displacement (MSD) of a Brownian particle, $\langle (x(t^*) - x(0))^2 \rangle$, grows linearly in time, with the slope being equal to $2D$, D being the diffusion coefficient, equation (3.7). Panel (c) shows simulations with $damp = 1$(green) and $damp = 5$(blue) and how they match up with the theoretical results(dashed colored lines), showing that increasing damp decreases the value of the diffusion constant, D, as it is related to increasing the friction constant γ. In panel (d) we see that increasing the value of temperature increases the value of the diffusion constant, D, as how the simulations with $T = 1$(green) and $T = 5$(blue) match with the theoretical results (dashed colored lines).

Chapter 4

Models for a binary mixture of Brownian oscillators

Nature gives us examples of complex synchronization behaviour where the oscillators are interacting with an ever changing swat of oscillators. From macroscale organization observed in flocking, where the oscillators phase is its the heading direction [21], to microscale organization where genetic clocks that can be controlled [49] and make bacteria blink at the same time [50]. In their 2017 work, Levis et al. [25], showed that the mobility is important for oscillators in these conditions and that various patterns can emerge. With these results in mind and wanting to find new behaviour that can give us control into the synchronization of these oscillators, we delved into what can be called a binary mixture of Brownian oscillators.

To be able to look into this problem we will have to use what we learned about the Kuramoto model and apply it to particles undergoing Brownian dynamics. This can be achieved by introducing a new internal degree of freedom, θ, that each particle will have and that will be governed by a modified Kuramoto model. We have some freedom in the way we define the mixture and we will look into two different models.

4.1 Model I - Repulsive interaction

The motion of our oscillators will be given by the Langevin dynamics described in the previous chapter, equation (5.4). We will be using LJ units as described in equations (3.10-3.12). In our first approach to the binary mixture of oscillators we split the oscillators into 2 categories, A and B, and changed the way they interact through the Kuramoto model:

$$\dot{\theta}_{i\in A} = \omega_i + \frac{1}{n_i}(\sum_{j\in A}^{n_i} K\sin(\theta_j - \theta_i) + \sum_{j\in B}^{n_i} H\sin(\theta_j - \theta_i)), \tag{4.1}$$

$$\dot{\theta}_{i\in B} = \omega_i + \frac{1}{n_i}(\sum_{j\in A}^{n_i} H\sin(\theta_j - \theta_i) + \sum_{j\in B}^{n_i} K\sin(\theta_j - \theta_i)), \tag{4.2}$$

where n_i represents the current number of neighbors of the particle i, and is determined by interaction range, R_θ, K and H are coupling constants that drive the interactions and that differentiate the interactions between same type particles and different type particles, K couples similar particles and H couples unlike particles. To reduce the complexity of the problem and to reduce the number of possible variables we fixed for the whole study the values of $R_\theta = 3$, in our dimensionless distance units, and we started by using $\omega_i = 0$ for every i. When K is positive and H is negative the phases of similar oscillators are attracted and the phases of different type oscillators are repelled and here we will be exploring the consequences of such choice. These equations are integrated using the Euler method with a timestep equal to the LAMMPS timestep, $dt = 0.01$, and the update is done before the forces are applied to the particles.

We will explore how this model behaves for different values of H, ranging from -0.001 to -1, and different values of K, 0.001 and 0.1. We will also explore different values of $\phi = \frac{N_B}{N_B+N_A}$, the number of B particles, N_B, over the total amount of particles, $N_B + N_A$, the parameter that controls how many repulsive pairwise contacts there are in the system, ranging from 0.05 to 0.95. For H or $K < 0.05$, all our simulations are done with $N = 1800$ and we will be looking at one different packing fractions, η, defined as $\eta = \frac{N\pi d^2}{4L^2}$, with d being the particles diameter, $d = \sqrt{2}^6$, using $L = 50$. For H or $K > 0.05$ we have $N = 1800$ and $N = 7200$ and we explore packing fractions ranging from 0.014 to 0.56. We found useful to use $\zeta = \frac{|H|}{K}$ as a parameter as it establishes a relationship between H and K.

We switch on the Kuramoto dynamics only after the system is at thermal equilibrium and we track the synchronization of the system by looking at a modified version of the order parameter, equation (2.2), by taking into account only the particles of one type, we are thus looking at how the addition of the phase repulsive interactions between the oscillators affect the synchronization of a specific group of oscillators. As the labels are arbitrary and the interactions are symmetric we focus on the synchronization of A particles:

$$|r(t^*)| = |\frac{1}{N_A}\sum_{j\in A}^{N_A} e^{i\theta_j(t^*)}|. \tag{4.3}$$

Our oscillators are not fully connected due to their short range interaction but their movement allows the network to continuously change over time, each oscillator exchanging its neighbours multiple times. Static networks of Kuramoto oscillators can sometimes not synchronize due to the network topology, but we observed that allowing the topology to change over time leads the system to synchronize. When the coupling constants are small, $-0.05 < H < 0$ and $0 < K < 0.05$ we can recover the time evolution predicted by mean field solution, and shown in figure 4.1(a), that is $r(t^*) \sim \frac{1}{\sqrt{1+e^{-\kappa(t^*-t_0)}}}$. This means that synchronization happens exponentially fast in the early times,$t^* < t_0 + \frac{1}{\kappa}$, and then r asymptotically approaches 1 at later times. This does not happen when the coupling constants are larger than 0.05. While in most simulations the value of the order parameter always increases over time it has more fluctuations and the shape of the time evolution is completely different from simulation to simulation, figure 4.1(c). After the order parameter grows above a certain threshold, $r \sim 0.8$, the shape of the time evolution of the order parameter is the same in all simulations and that can be well fit with the theoretical curve, seen in figure 4.2(c). Looking at panels (a)-(d) and (e)-(h) of figure 4.2 we can see the main difference between these cases. Panels (a)-(d) show the time evolution of the order parameter followed by snapshots of the oscillators phases at a given time for $H = -0.001$ and $K = 0.001$, and panels (e)-(h) show the same but for $H = -0.1$ and $K = 0.1$. In the latter case it is possible to observe the formation of vortices. The value of the coupling constant above which vortices appear may be related to the density of oscillators, the radius of interaction and with the ability of the oscillators to explore space, but these parameters were not studied.

The mean field result discussed previously predicts that $\kappa = K$ and that $t_0 \propto \frac{1}{K}$ but the addition of a second type of oscillators changes this behaviour and κ and t_0 become functions of K, H and ϕ.

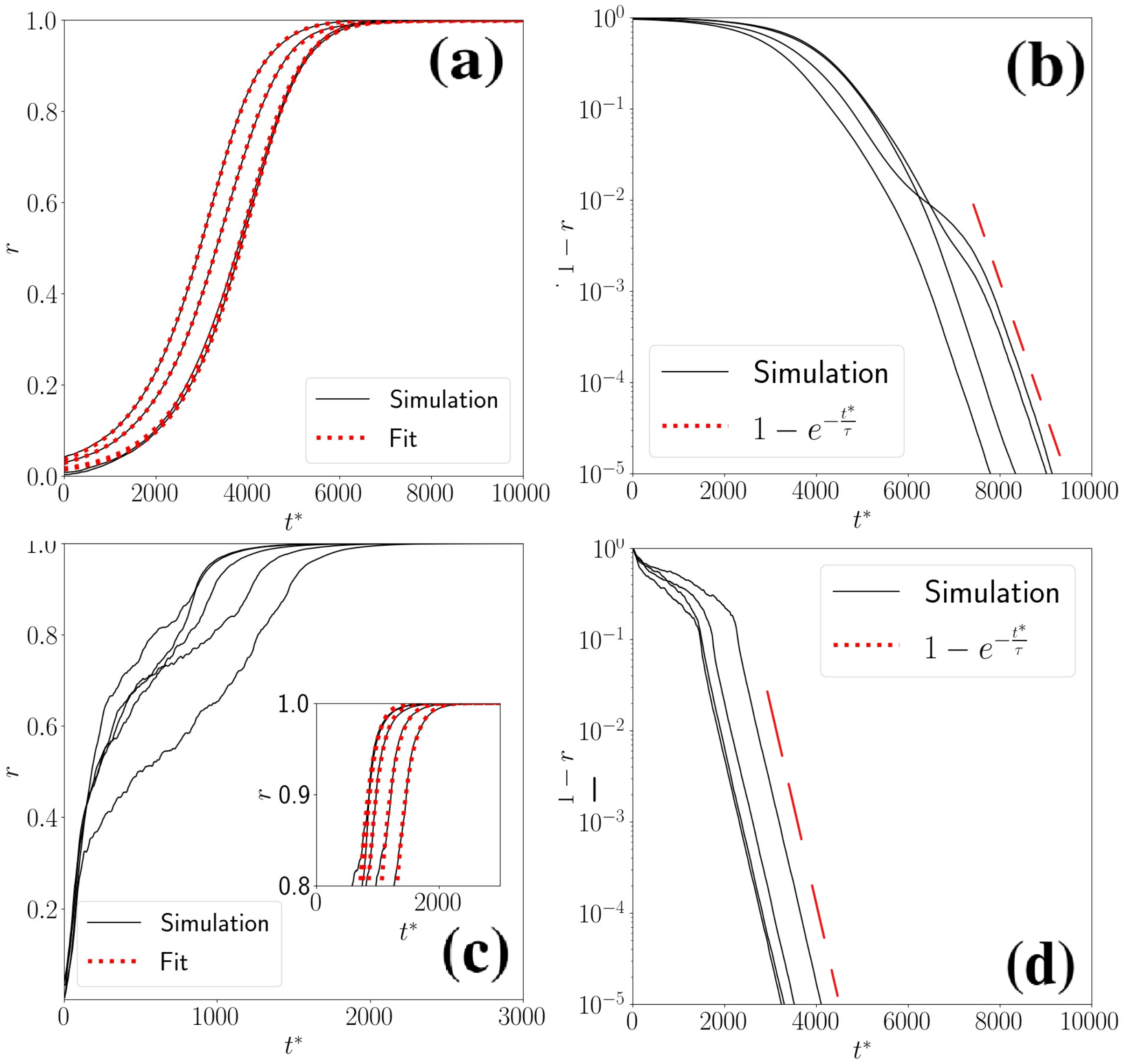

Figure 4.1: **Time evolution of the order parameter.** Panels (a) and (c) show the time evolution of the order parameter for systems with N = 1800, $\phi = 0.5$, $K = 0.001$ and $H = -0.001$ and -0.1 respectively. The red curve is the fitted curve for $r(t^*) \sim \frac{1}{\sqrt{1+e^{-\kappa(t^*-t_0)}}}$. Panels (b) and (d) show the time evolution of $1-r$, highlighting the late time $r(t^*) \sim 1-e^{-\frac{t*}{\tau}}$ .Panel (a) shows how different initial conditions give the same qualitatively behaviour while (c) shows that each initial condition has a different behaviour qualitatively. Panels (b) and (d) show how the late time behaviour is similar for all initial conditions.

By plotting κ as a function of ϕ, see figure 4.3(a), we observe that an increase of the value of H leads to an increase of κ which depends on ϕ. When $K = |H|$, κ does not seem to significantly change with ϕ, but when $|H| > K$, κ grows for a maximum around $\phi = 0.5$, decreasing again for higher ϕ. The almost symmetric shape is a result of the interaction between the two types of oscillators and as soon as one of the types is fully synchronized the other quickly follows. By plotting t_0 as a function of ϕ, like in figure 4.3(b), we observe that a increase of the value of H leads to a decrease of t_0 which depends on ϕ. When $K = |H|$, t_0 does not seem to significantly change with the value of t_0, but when $|H| > K$, t_0 decreases to a minima around $\phi = 0.5$, increasing again for high ϕ. The almost symmetric shape again follows from the fact that the synchronization of each group of oscillators happens at the same time. Although this behaviour is similar to what one expects, an increase of H leads to an increase of κ and a decrease of t_0 we could not find an expression for $\kappa(H, \phi)$ or $t_0(H, \phi)$.

Plotting κ as a function of ζ for different values of ϕ, as figure 4.4(a) shows an increase of the value

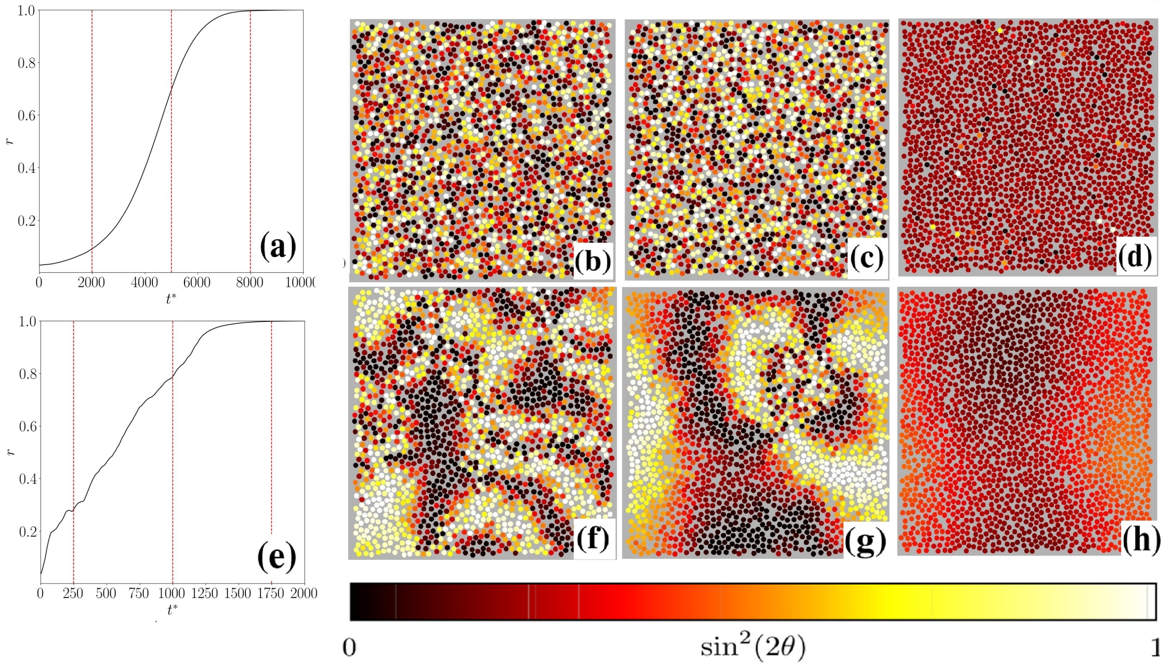

Figure 4.2: **Snapshots of the time evolution of the system.** Panels (a) and (e) show the time evolution of the order parameter for systems with N = 1800, $\phi = 0.5$, $K = 0.001$ and $H = -0.001$ and -0.1 respectively. Panels (b) to (d) show the same system of panel (a) with each panel being at the time respective to the dashed lines in panel (a), and panels (f) to (h) show the same system of panel (e) with each panel being at the time respective to the dashed lines in panel (e). The color scheme used for the phase to the oscillators is chosen as to better display the vortices observed. Both systems reach a synchronized state, $r \sim 1$, and an almost uniform coloring is observed in panels (d) and (h).

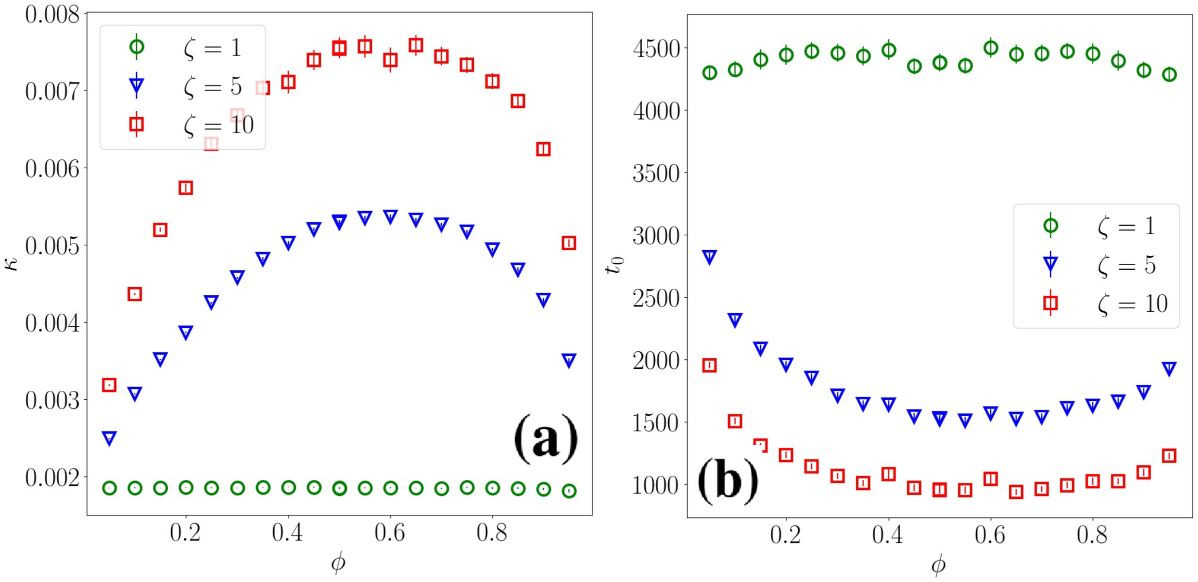

Figure 4.3: **Dependence of κ and t_0 on ϕ.** Panel (a) shows the dependence of κ on ϕ for various values of ζ, by varying the value of H. Panel (b) shows the dependence of t_0 on ϕ for various values of ζ, by varying the value of H. In all cases, $K = 0.001$ and $N = 1800$.

of κ as the value of ζ increases and that there is a dependence on ϕ. We see the opposite happen when when plotting t_0 as a function of $zeta$ for different values of ϕ, see figure 4.4(b).

For values of K or H larger than 0.05 we can not calculate the value of κ or t_0 due to the way the order parameter grows in time. In the course of the system evolution we observe Schlieren patterns that are normally seen in systems with broken rotational symmetry, like liquid crystals. We also notice a

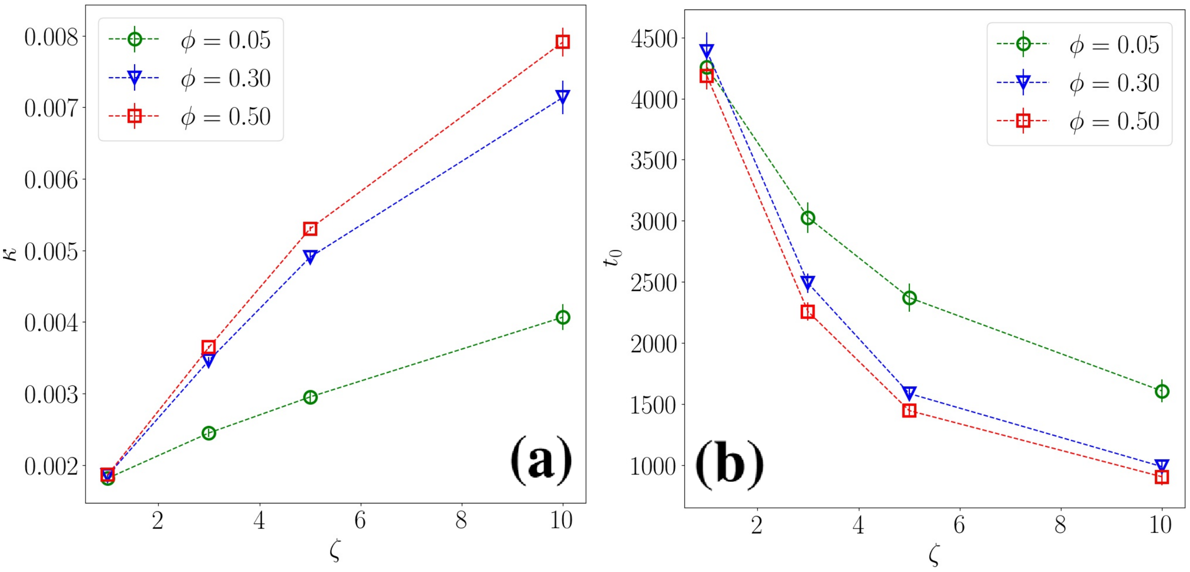

Figure 4.4: **Dependence of κ and t_0 on ζ.** Panel (a) shows the dependence of κ on ζ for various values of ϕ. Panel (b) shows the dependence of t_0 on ζ for various values of ϕ in a log-log scale, In all cases, $K = 0.001$ and $N = 1800$.

coarsening sequence similar to the one observed in a 2D XY-model upont a temperature quench $T = \infty$ to $T = 0$ showing that the presence of contrarian oscillators does not disrupt the synchronization process of A-type oscillators, as we observe the growth of synchronized regions until they span the whole system, as seen in figure 4.5. At later times when all the vortices of opposite topological charge annihilate each other, the order parameter grows like $r = 1 - e^{\frac{-t^*}{\tau}}$, like figure 4.2(d) demonstrates, τ being a characteristic time that depends on ζ, η and ϕ.

The late time behaviour is almost symmetrical around $\phi = 0.5$, with τ having a minimum value when $\zeta > 1$, a maximum value when $\zeta < 1$ and staying constant for $\zeta = 1$, as shown in figure 4.6(a).

The synchronization characteristic time τ displays a power law dependence on $|H|$ with the exponent depending on ϕ, as shown in figure 4.6(b). This power law dependence is observed when $\zeta > 10$, with the exponent reaching the maximum absolute value at $\phi = 0.5$.

When comparing $\frac{\tau}{N}$ for systems with different numbers of particles, but with similar η we see that the results match quite well, meaning that $\tau \propto N$, seen in figure 4.7(a). It is also possible to see a non-monotonic behaviour of τ on η depending on the value of ζ, as shown in figure 4.7(b). At lower packing fractions, oscillators will interact rarely due to their interaction being close range but at high enough packing fraction the steric interactions will jam the system, making the particles exchange neighbours less often, leading to a slower mixing process. As ζ grows the effect of reduced mobility is less important.

We calculated t_c which is the average time it takes the oscillators to reach their almost complete synchronization, $r > 0.95$. By plotting t_c as a function of ϕ, like in figure 4.8(a) it is possible to observe that increasing ζ decreases the value of t_c. If we plot t_c as a function of ζ, as in figure 4.8(b) we see that value of t_c seems constant when $\zeta < 1$ as the synchronization is mostly driven by the value of the highest coupling constant, that in this case is K.

Model I shows novel ways to control synchronization. By introducing the ”repulsive” oscillators it is possible to enhance how the rate of synchronization, both by increasing the value of $|H|$ or by bringing the value of ϕ closer to 0.5. Controlling the density of oscillators is also a way to enhance synchronization as the mobility of the oscillators plays a significant role. It was impossible to completely stop synchronization with this model and we will be looking at a different formulation of the Kuramoto

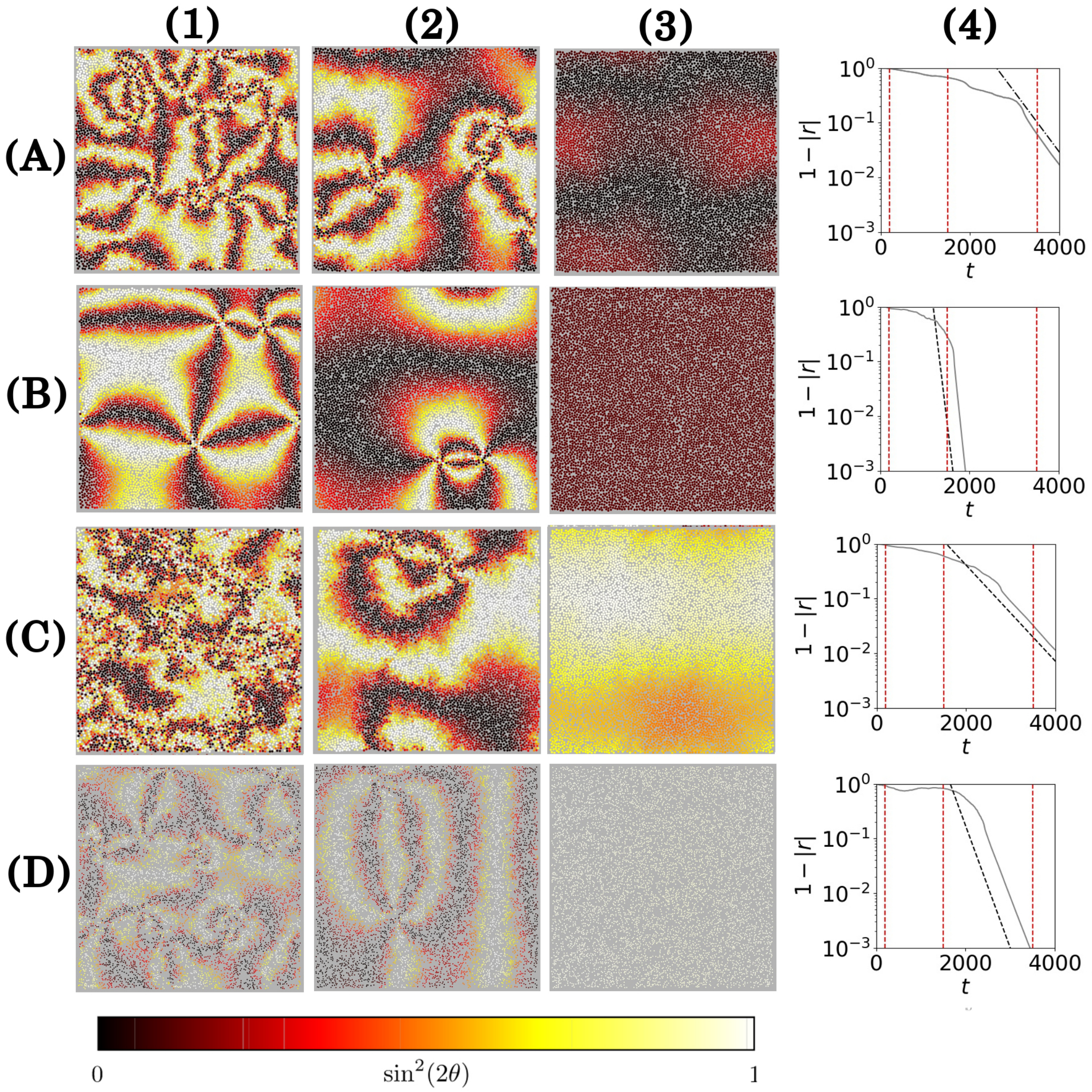

Figure 4.5: **Snapshots of some systems.** The snapshots show the time evolution of the system from (1) to (3)(t^* = 200, t^*=1500, t^*=3500 respectively). Different letters have the same initial conditions but different parameters: (A) has $\zeta = 20$, $\eta = 0.56$, $\phi = 0$, (B) has $\zeta = 20$, $\eta = 0.56$, $\phi = 0.5$,(C) has $\zeta = 0.1$, $\eta = 0.56$, $\phi = 0.5$, (D) has $\zeta = 20$, $\eta = 0.14$, $\phi = 0.5$ and in all cases N=7200.

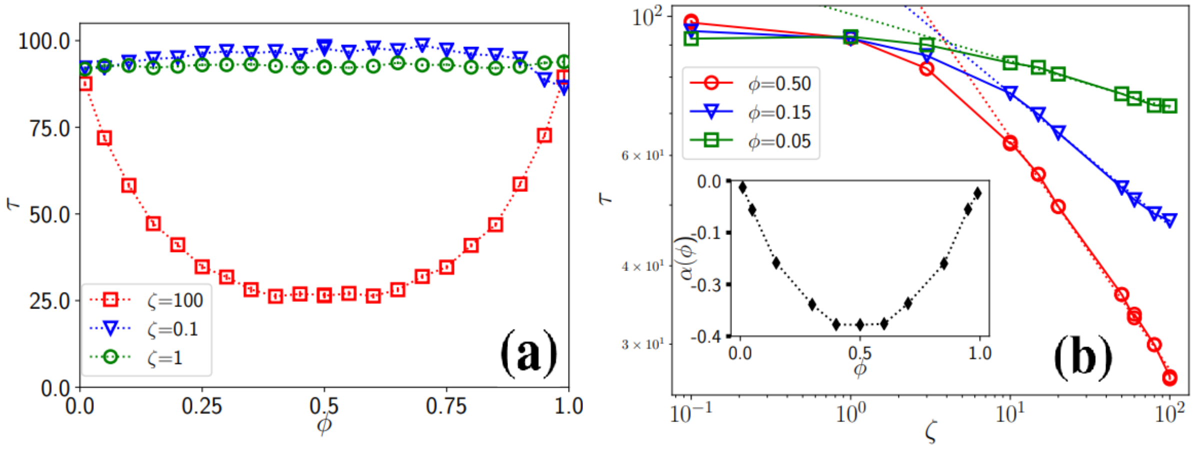

Figure 4.6: **Dependence of τ on ϕ and ζ.** Panel (a) shows that the synchronization characteristic time, τ increases as a function of ϕ. It is symmetrical at $\phi = 0.5$ decreasing to the same value for values of $\zeta < 1$. For values of $\zeta > 1$ the opposite is true, decreasing as a function of ϕ until $\phi = 0.5$, after that increasing to close its starting value. When $|H| = K$ τ doesn't depend on ϕ. Panel (b) shows that when $\zeta > 10, \tau \propto \zeta^{\alpha(\phi)}$. The dependence of α on ϕ is shown in the inset.In all cases, $\eta = 0.14$, $N = 1800$, $K = 0.1$.

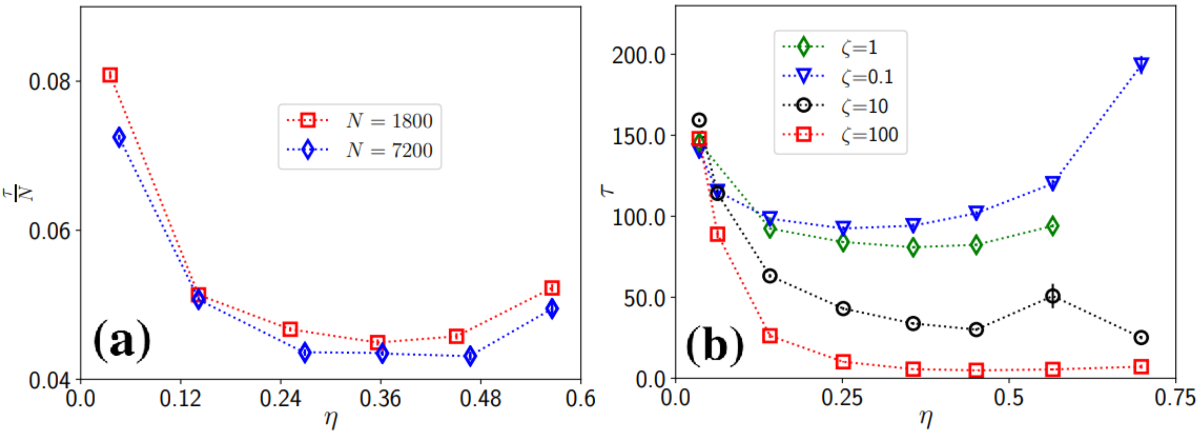

Figure 4.7: **Characteristic time dependence on η.** Panel (a) shows that if the characteristic time is rescaled by N it is possible to observe the same dependence of $\frac{\tau}{N}$ with η. In panel (b) we see that for the same ζ, N and ϕ but different η the system has a packing fraction that minimizes τ, due to the balance of short range interactions and mixing capability

model to achieve this.

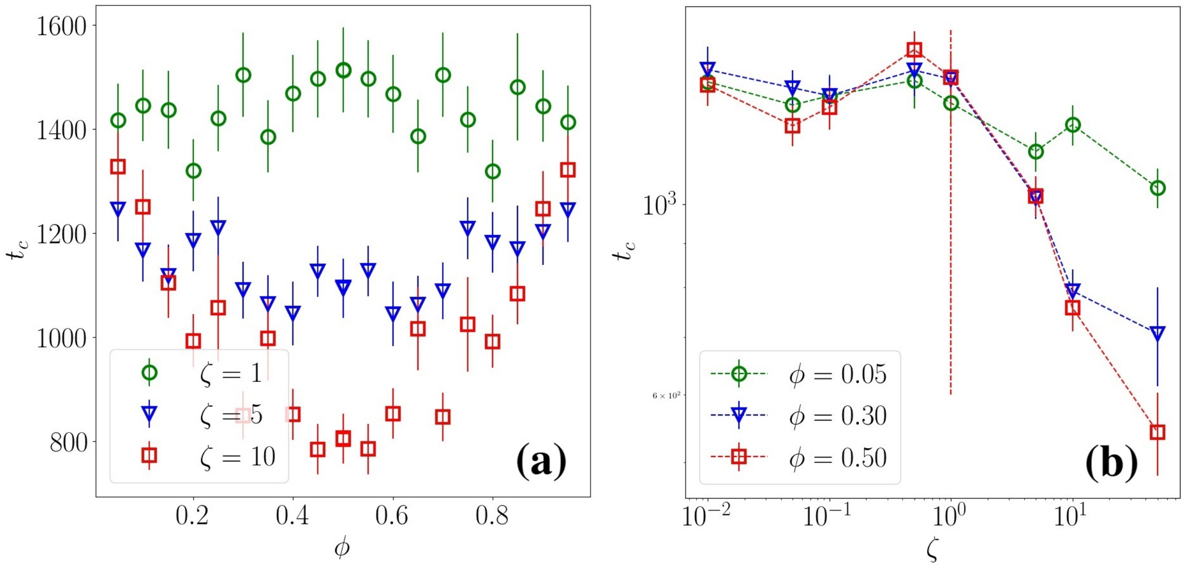

Figure 4.8: **Dependence of t_c with ϕ and ζ.** Panel (a) shows the dependence of t_c on ϕ for various values of ζ, by varying the value of H. Panel (b) shows the dependence of t_c on ζ for various values of ϕ. For all cases $K = 0.1$ and $N = 1800$.

4.2 Model II - Contrarian oscillators

With model II the oscillators are split into 2 categories, A and B, and the Kuramoto interaction is given by:

$$\dot{\theta}_{i\in A} = \omega_i + \frac{1}{n_i}(\sum_{j\in A}^{n_i} K\sin(\theta_j - \theta_i) + \sum_{j\in B}^{n_i} H\sin(\theta_j - \theta_i)), \tag{4.4}$$

$$\dot{\theta}_{i\in B} = \omega_i + \frac{1}{n_i}(\sum_{j\in A}^{n_i} H\sin(\theta_j - \theta_i) + \sum_{j\in B}^{n_i} H\sin(\theta_j - \theta_i)), \tag{4.5}$$

where n_i represents the current number of neighbors of the particle i, is determined by a fix interaction range,R_θ, K and H are coupling constants that drive the interaction. In this model, particles of the B type act as contrarians, not trying to synchronize with other B particles nor with A particles, this being the main difference from model I described in the previous subsection. To reduce the complexity of the problem and to reduce the number of possible variables we fixed for the whole study the values of $R_\theta = 3$, in our dimensionless distance units, and we started by using $\omega_i = 0$ for every i. These equations are integrated using the Euler method with a timestep equal to the LAMMPS timestep, $dt = 0.01$, and the update is done before the forces are applied to the particles. We will also explore different values of $\phi = \frac{N_B}{N_B+N_A}$, the fraction of B particles, N_B, over the total amount of particles, $N_B + N_A$, the parameter that controls how many repulsive oscillators there are in the system, ranging from 0.05 to 0.95. All our simulations are done with $N = 1800$ and and a box size $L = 100$.

We switch on the Kuramoto dynamics only after the system is at thermal equilibrium and we track the synchronization of the system by looking at a modified version of the order parameter in, equation (2.2). While in model I the labels of the particles are arbitrary now particles of the type A have a positive interaction between themselves and a negative one with particles of type B and particles of type B have an overall negative interaction. A system with similar characteristics has been considered in reference [16], were this interaction managed to suppress synchronization in a fixed network of oscillators. As figure 4.9 shows it is possible to completely suppress synchronization of both types of particles by increasing the value of $|H|$.

While the value of $r_\infty \equiv r(t^* \to \infty)$, of model I is always 1, model II shows a dependence of r_∞ on H, K and ϕ. There is a continuous configurational transition governed by the H and ϕ, where the value of r_∞ measured on particles of type A and type B decreases from 1 to 0, that is there is a configurational transition from synchronizable configurations to unsynchronizable ones driven by either ϕ or H, as observed in figure 4.10(a-b).

For $H = -1$ we plot the value of r_∞ for particles of type A and type B. The curve for the particles A reassembles the curve of the spontaneous magnetization of the Ising model with ϕ taking the role of temperature, seen in figure 4.11(a). The curve for particles of type B reassembles the curve o spontaneous magnetization of the Ising model with ϕ taking the role of temperature and with a magnetic field applied, as observed in figure 4.11(b). The synchronization behaviour of the system is presented in figure 4.12, with the particles of type A, managing to synchronize, panels (a)-(c), for small values of $|H|$, $H = -0.001$, even though particles of type B not displaying any sign of synchronization, panels (d)-(f). For high values of $|H|$, $H > 10$, particles of both types show no sign of synchronization, no discernible patterns emerging as time evolves.

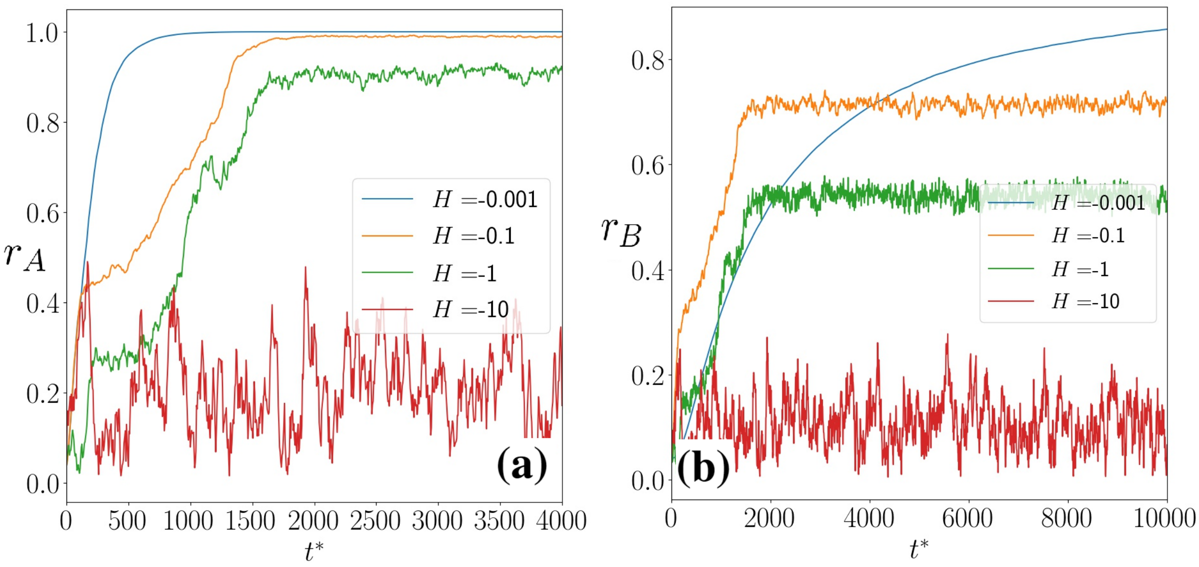

Figure 4.9: **Time evolution of the order parameters for model II.** Panel (a) shows the value of the order parameter for particles of type A and panel (b) shows the value of the order parameter for particles of type B. For values of $|H| < 0.1$ synchronization happens like in model I, the system fully synchronizing after a given time. For values of $|H| > 0.1$ both A and B particles reach a saturation value, r_∞ smaller than 1, the system never fully synchronizing. For even larger values of $|H|$, $|H| = 10$, the order parameter behaves erratically and the system never synchronizes. All simulations were done with $K = 0.001$ and $\phi = 0.5$

.

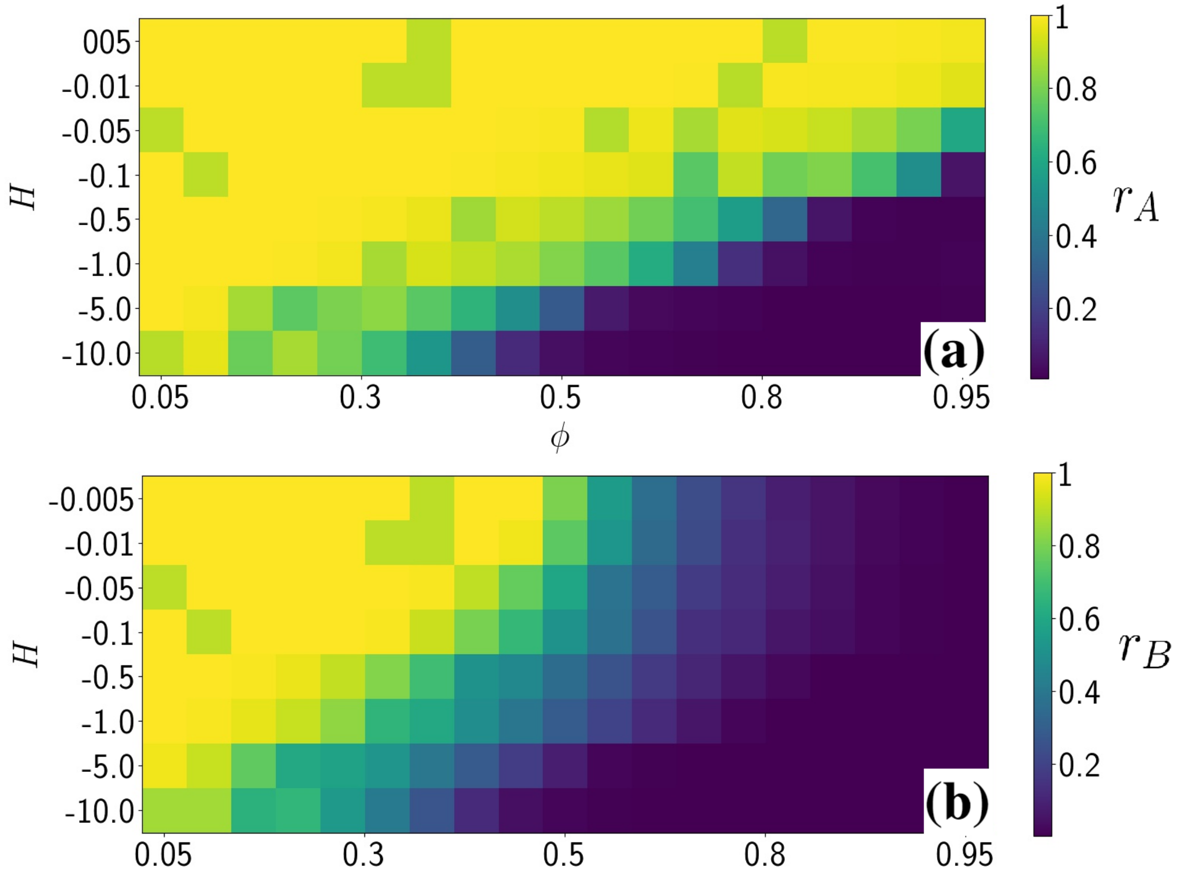

Figure 4.10: **Phase diagram for the value of r_∞.**Panel (a) shows the value of r_∞ for particles of type A and panel (b) shows the value of r_∞ for particles of type B. It is possible to observe a continuous configurational transition as the value of r_∞ goes from 1 to 0. The value of r_∞ is different for particles of type A, panel (a) and for particles of type B, panel (b) and the values of ζ or ϕ that suppress their synchronization are lower for particles of type B. All simulations were done with $K = 0.1$.

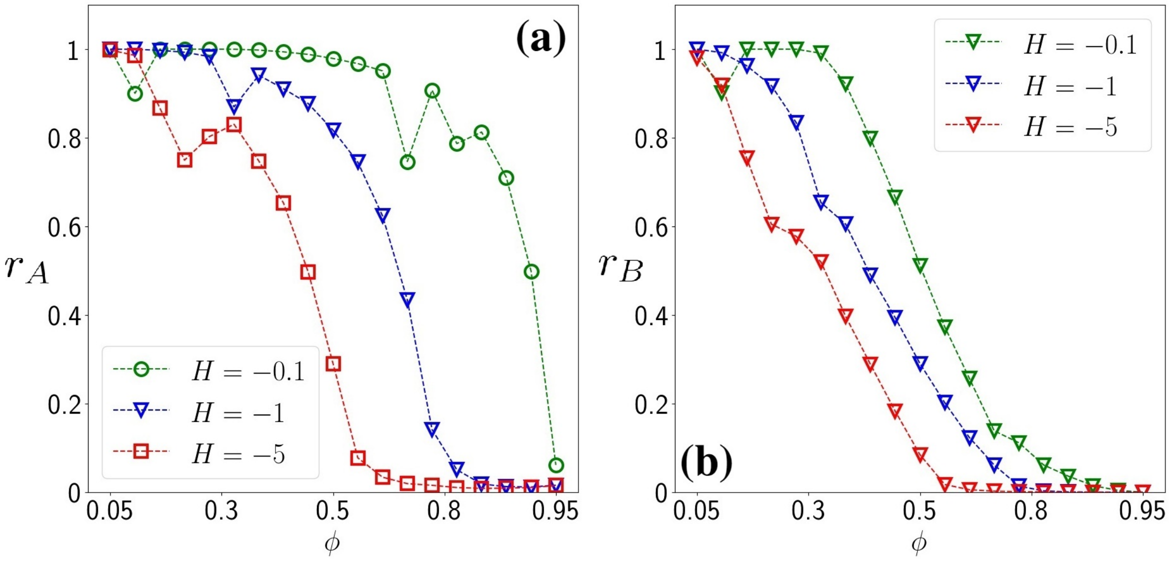

Figure 4.11: **Dependence of $r_{a\infty}$ and $r_{b\infty}$ on ϕ.** In panel (a) we see the decrease of $r_{a\infty}$ as ϕ increases. In panel (b) we see the same decrease of $r_{b\infty}$ as ϕ increases. In both cases $N = 1800$, $H = -1$ and $K = 0.1$.

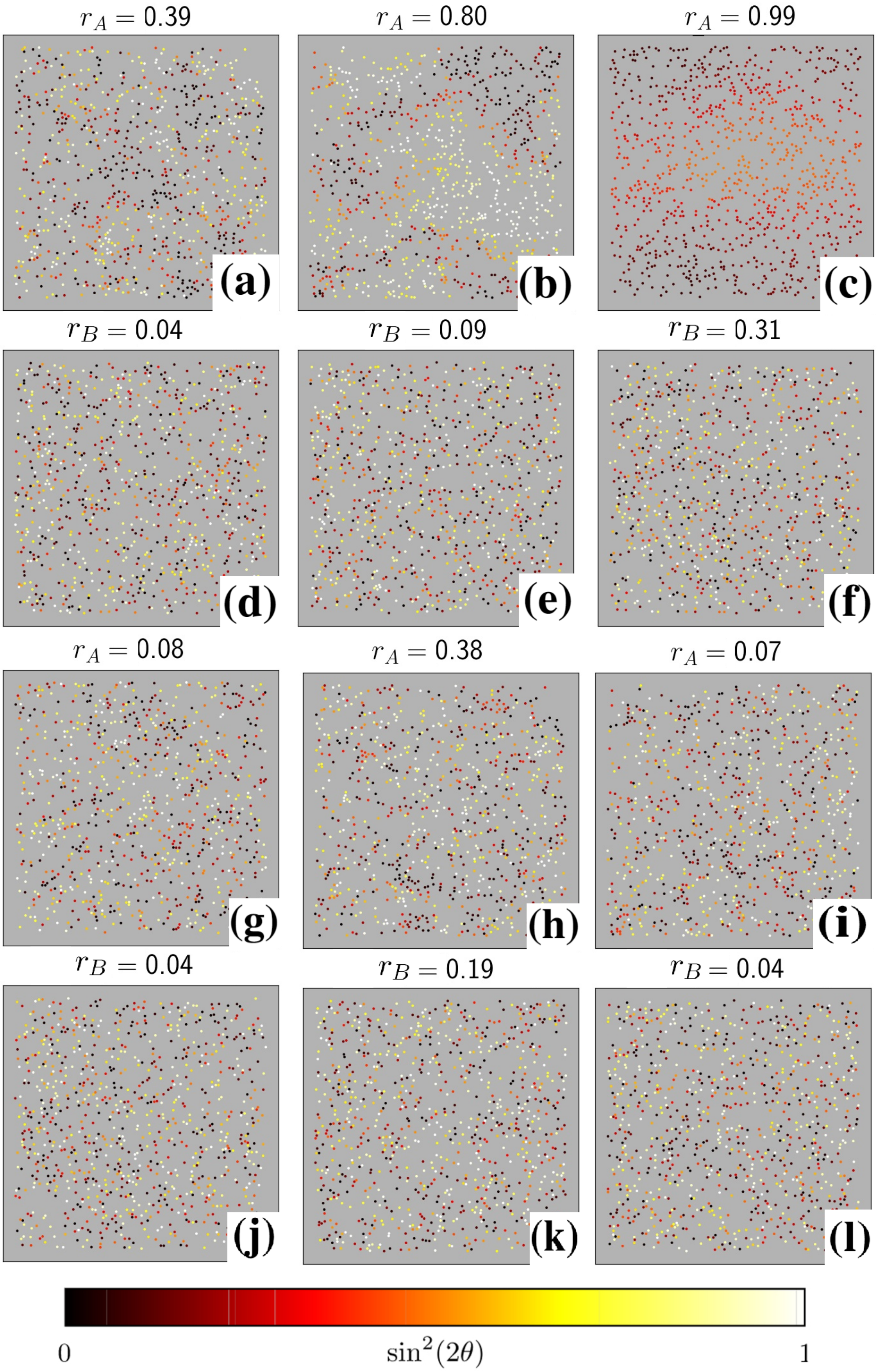

Figure 4.12: **Snapshots of the time evolution of Model II.** Panels (a)-(l) show snapshots with particles A and B separated, top and bottom plot respectively, to better distinguish their behaviour. Plots (a)-(c) show synchronization of the particles of type A, $r = 0.39$, 0.8 and 0.9 respectively, while the particles of type B remain unsynchronized, $r < 0.4$ in panels (d)-(f), due to the small value of H, $H = -0.001$. Plots (g)-(h) show how high values of $|H|$, $H = -10$, completely stop synchronization from happening as the value of r fluctuates for particles of both types, going as high as 0.38 but staying around $r = 0.2$. For all, $K = 0.1$, $N = 1800$ and $\phi = 0.1$

Chapter 5

Active Brownian Motion

5.1 Analytic results

Some behaviour of small swimmers (μm) can be captured by the use study of active Brownian particles. Due to the fact that these particles extract energy from the environment to produce motion and because they have a preferred direction of motion they break detailed balance and are an out-of-equilibrium system. They are still subject to thermal fluctuations so their behaviour can be expressed by the Langevin equations. Due to the small mass of the particles we will not take into account the inertial terms and will work in the so called overdamped regime. The equation of motion for a ABP moving in two dimensions is then:

$$\begin{aligned} \dot{x}(t) &= v_p \cos(\theta(t) + F_x, \\ \dot{y}(t) &= v_p \sin(\theta(t)) + F_y, \\ \dot{\theta}(t) &= F_\theta, \end{aligned} \tag{5.1}$$

Where F_x, F_y are the components of the translational noise acting on the particle in the x and y direction respectively and F_θ is the rotational noise and v_p is the particle self-propulsion velocity. The Stokes-Einstein relation gives an expression for the translational diffusion constant $D = \frac{k_b T}{\gamma}$, where k_b is the Boltzmann constant, T is the temperature of the fluid the particle is immersed in, and γ is the Stokes coefficient, which is related to the drag the fluid exerts in the particle. And the Einstein–Smoluchowski relation gives an expression for the rotational diffusion constant $D_r = \frac{k_b T}{f_r}$, where f_r is the frictional rotational drag. An active particle will tend to move in a specific direction during a specific time τ_R which is related to the diffusion constant of rotation D_R by $D_R = \frac{1}{\tau_R}$. The mean square displacement can be shown, as was done in Bechinger work in 2016, to be given by:

$$\langle (r(t) - r_0)^2 \rangle = (4D + 2v_p^2 \tau_R)t + 2v_p^2 \tau_R^2 (e^{\frac{-t}{\tau_R}} - 1) \tag{5.2}$$

Which for times bigger than the rotational relaxation time τ_R reduces to:

$$\begin{aligned} \langle (r(t) - r_0)^2 \rangle &= (4D + 2v_p^2 \tau_R)t \\ &= 4D_{eff} t, \end{aligned} \tag{5.3}$$

with an effective diffusion constant $D_{eff} = D + \frac{v_p^2}{2D_R}$. This means that for long timescales active particles display a diffusive behaviour with an a higher effective diffusion constant.

5.2 Examples

The dynamics of living micro-swimmers like spermatozoa or bacteria can be studied using this model and it is possible to make artificial active Brownian particles like Janus particles [5], which are cylindrical rods that are coated with 2 different metals gold–platinum (Au–Pt) or gold–nickel (Au–Ni) that when immersed in hydrogen peroxide (H2O2) solutions will display directed motion. these particles have a preferred direction of motion, towards the direction the platinum part of the rod, as shown in figure 5.1, however the direction of motion changes in time, such that these particles exhibit active Brownian behaviour.

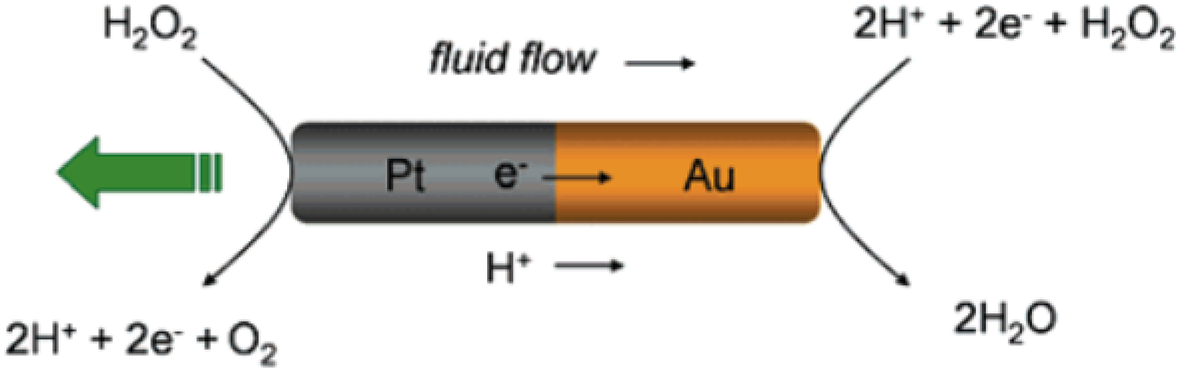

Figure 5.1: A schematic illustrating self-electrophoresis. Hydrogen peroxide is oxidized to generate protons in solution and electrons in the wire on the Pt end. The protons and electrons are then consumed with the reduction of H_2O_2 on the Au end. The resulting ion flux induces motion of the particle relative to the fluid, propelling the particle toward the platinum end with respect to the stationary fluid. Taken with permission from [5].

Active particles are known to show complex out-of-equilibrium behaviour, like motility induced phase separation (MIPS) [6], where the introduction of activity to Brownian particles makes them cluster into what can be called ”living crystals”, as can be observed in figure 5.2, that appear depending on the system density and activity. This kind of behaviour is also observed in colonies of bacteria [51] [52], showing how useful this model is in describing the behaviour of living organisms.

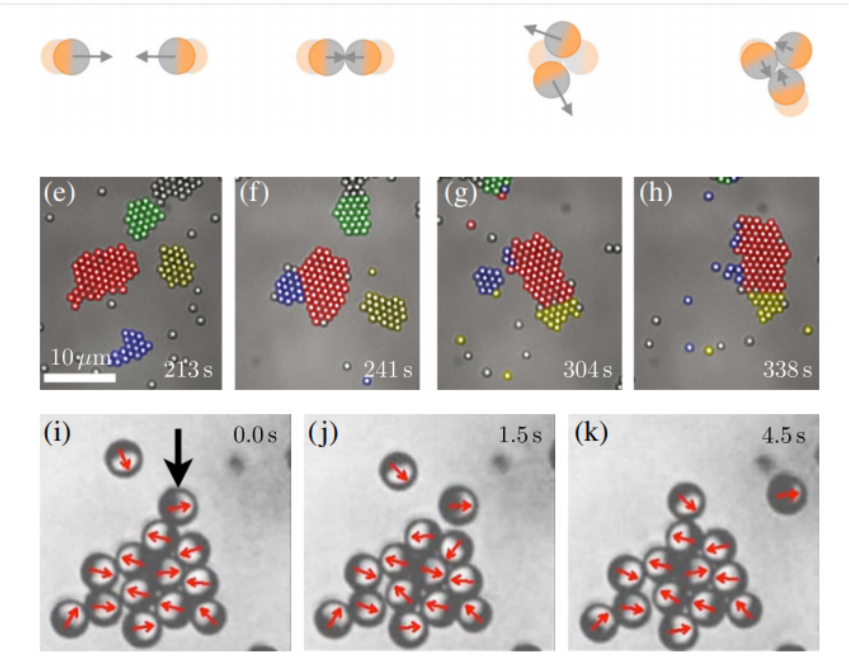

Figure 5.2: Living crystals formed by clusters: due to the motility of theseJanus particles it is possible to observe a phase segregation into the dense, crystal-like phase, and the dilute, gas-like phase. Taken with permission from [6].

5.3 Simulations

We again used LAAMPS as a library to perform molecular dynamics. LAMMPS applies a Langevin thermostat as described in [47] modeling a background implicit solvent and performing constant NVE integration, where N stands for the number of particles, V for volume and E for energy,[48]. LAMMPS integrates these equations of motion using the Verlet method:

$$\begin{aligned} m\ddot{\vec{r_i}} &= -\nabla U(\vec{r_i}) + \vec{F_f^i} + \vec{F_r^i} + \vec{F_a^i}, \\ U(\vec{r_i}) &= \begin{cases} \sum_j 4\epsilon[(\frac{\sigma}{r_{ij}})^{12} - (\frac{\sigma}{r_{ij}})^6], |\vec{r_i} - \vec{r_j}| < \sqrt[6]{2}, \\ 0, r_{ij} > \sqrt[6]{2}. \end{cases} \\ \vec{F_f^i} &= -\frac{m}{damp}\vec{v}, \\ \vec{F_r^i} &\propto \sqrt{\frac{k_B T m}{dt * damp}}, \\ \vec{F_a^i} &\propto v_p \cos(\theta_i)\vec{u_x} + v_p \sin(\theta_i)\vec{u_y}, \\ \dot{\theta}_i &= F_\theta \end{aligned} \tag{5.4}$$

where the index i indicates the index of the particle, the position of the particle,$U(\vec{r_i})$ is the Lennard-Jones potential, with ϵ being the depth of the potential and σ, diameter of a particle, is the viscous drag term that is proportional to the particle velocity $\vec{v}$, $\frac{m}{damp}$ taking the place of the friction constant, with m being the mass of the particle and $damp$ being a constant inversely related to the viscosity of the solvent. $\vec{F_r^i}$ is the random force that the particle feels due to the solvent atoms and $dt = 0.01$ being the simulation timestep. $\vec{F_a^i}$ is the propulsion force, being proportional to the propulsion velocity, v_p with an heading given by the vector $cos(\theta_i)\vec{u_x} + sin(\theta_i)\vec{u_y}$, with u_x and u_y being the unitary vectors on those directions, the value θ_i changing due to a random number, F_θ. We use Leonard-Jones units, where the fundamental quantities m, mass of a particle, σ, radius of a particle,ϵ depth of the Lennard-Jones well, and k_b are all equal to 1, as described in, equation (3.10-3.12).

Active particles move in straight trajectories during time intervals smaller than their rotational relaxation time, $\tau_\theta = \frac{1}{D_\theta}$, as can be observed in figure 5.3(a). The long time, $t^* > \frac{1}{D_{eff}}$, diffusive behaviour and the short time, $t^* < \frac{1}{D_\theta}$ ballistic behaviour of the active particle were also observed, see figure 5.3(b), by plotting the mean square displacement of a particle. By plotting the mean square displacement (MSD) with different propulsion velocities, like in figure 5.3(c) we were able to reproduce the theoretical diffusion coefficient that was expected, equation 5.3.

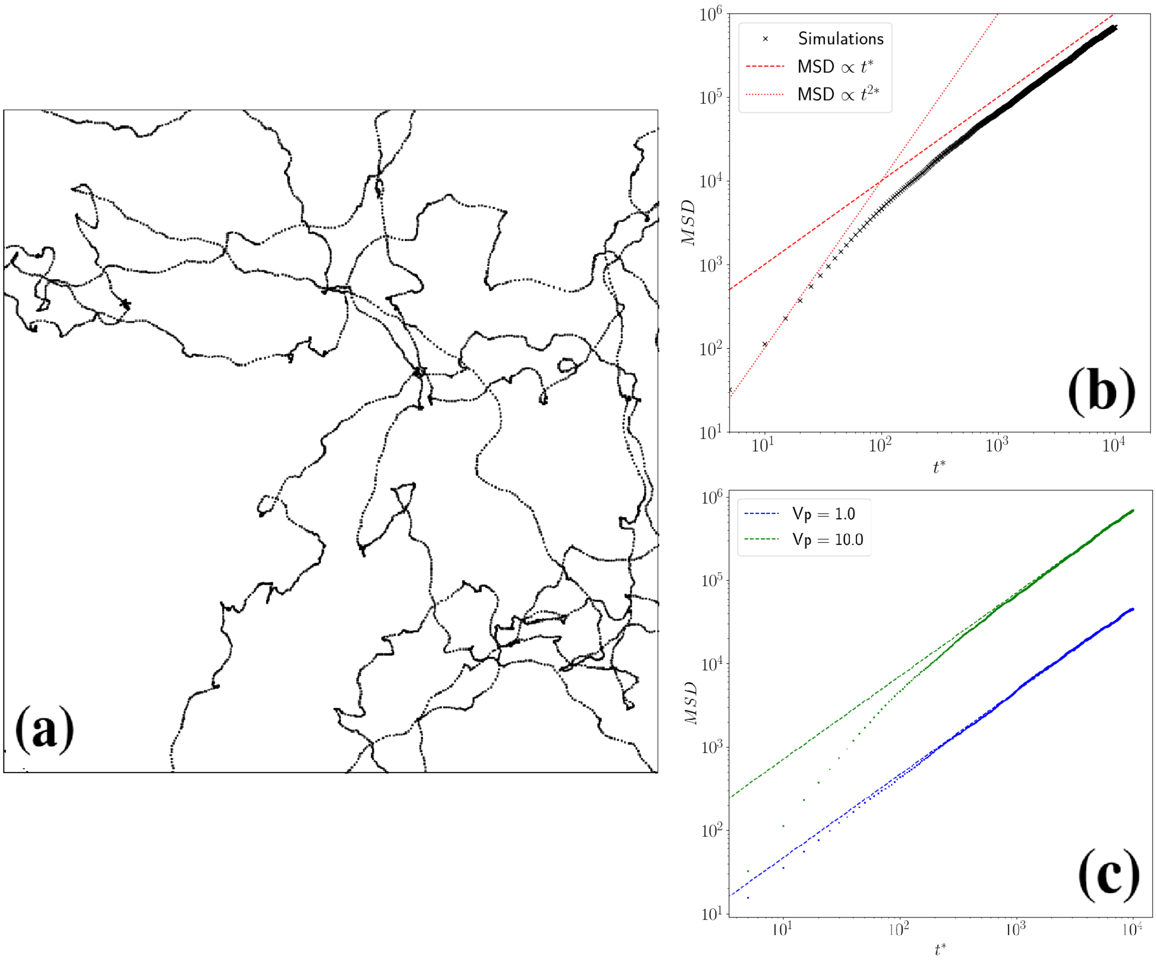

Figure 5.3: **Behaviour of a active Brownian particle.**In panel (a) we can see the trajectories of an active Brownian particle moving in a 50x50 box with periodic conditions. In panel (B) the mean square displacement (MSD) of a Brownian particle, $\langle (x(t^*) - x(0))^2 \rangle$, grows linearly in time, with the slope being equal to $2D$, D being the diffusion coefficient, equation (3.7), after a ballistic regimen where the mean square displace grows quadractically in time. Panel (c) shows simulations with $vp = 10$(green) and $vp = 1$(blue) and how they match up with the theoretical results(dashed colored lines), showing that increasing the propulsion velocity, v_p, increases the value of the diffusion constant, D, according to equation 5.3).

Chapter 6

Active model I: a model for a binary mixture of active Brownian oscillators

Interested in the potential of active particles and the different ways that these particles can display non-trivial collective behaviour, we decided to bring together what we described in the chapter of active particles with what was described with the Kuramoto model. We again used LAAMPS as the library that handled the molecular dynamics simulations. The dynamics of our active particles were given by equations:

$$\begin{aligned}
m\ddot{\vec{r_i}} &= -\nabla U(\vec{r_i}) + \vec{F_f^i} + \vec{F_r^i} + \vec{F_a^i}, \\
U(\vec{r_i}) &= \begin{cases} \sum_j 4\epsilon[(\frac{\sigma}{r_{ij}})^{12} - (\frac{\sigma}{r_{ij}})^{6}], |\vec{r_i} - \vec{r_j}| < \sqrt[6]{2}, \\ 0, r_{ij} > \sqrt[6]{2}. \end{cases} \\
\vec{F_f^i} &= -\frac{m}{damp}\vec{v}, \\
\vec{F_r^i} &\propto \sqrt{\frac{k_B T m}{dt * damp}}, \\
\vec{F_a^i} &\propto v_p \cos(\theta_i)\vec{u_x} + v_p \sin(\theta_i)\vec{u_y}.
\end{aligned} \tag{6.1}$$

and the evolution of the phase of each particle, θ, was given by the Kuramoto equations they were defined in model I:

$$\begin{aligned}
\dot{\theta}_{i\in A} &= \omega_i + \frac{1}{n_i}(\sum_{j\in A}^{n_i} K \sin(\theta_j - \theta_i) + \sum_{j\in B}^{n_i} H \sin(\theta_j - \theta_i)) + F_\theta, \\
\dot{\theta}_{i\in B} &= \omega_i + \frac{1}{n_i}(\sum_{j\in A}^{n_i} H \sin(\theta_j - \theta_i) + \sum_{j\in B}^{n_i} K \sin(\theta_j - \theta_i)) + F_\theta.
\end{aligned} \tag{6.2}$$

For the equations of motion, eq. (6.1), the index i indicates the index of the particle, the position of the particle,$U(\vec{r_i})$ is the Lennard-Jones potential, with ϵ being the depth of the potential and σ, diameter of a particle, is the viscous drag term that is proportional to the particle velocity $\vec{v}$, $\frac{m}{damp}$ taking the place of the friction constant, with m being the mass of the particle and $damp$ being a constant inversely related to the viscosity of the solvent. $\vec{F_r^i}$ is the random force that the particle feels due to the solvent atoms and $dt = 0.01$ being the simulation timestep. $\vec{F_a^i}$ is the propulsion force, being proportional to the propulsion velocity, v_p with an heading given by the vector $cos(\theta_i)\vec{u_x} + sin(\theta_i)\vec{u_y}$, with u_x and u_y being the unitary vectors on those directions, the value θ_i changing due to a random number, F_θ. For the phase equation, eq. (6.2) where n_i represents the current number of neighbors of the particle i, and is determined by interaction range, R_θ, K and H are coupling constants that drive the interactions and that differentiate the interactions between same type particles and different type particles, K couples similar particles and H couples unlike particles, and F_θ is a rotational noise term. To reduce the complexity of the problem and to reduce the number of possible variables we fixed for the whole study the values of $R_\theta = 3$, in our dimensionless distance units, and we started by using $\omega_i = 0$ for every i. We use Leonard-Jones units, where the fundamental quantities m, mass of a particle, σ, radius of a particle,ϵ depth of the Lennard-Jones well, and k_b are all equal to 1, as described in, equation (3.10-3.12).The equations for the phase of the oscillators are integrated using the Euler method with a timestep equal to the LAMMPS timestep, $dt = 0.01$. LAMMPS is designed to have its iterative scheme done in a specific order, like the creation of neighboring lists, the calculation of the forces to be applied and the time integration, and the update of the phases is done before the forces are applied to the particles. We explored values of K and $|H| = 0.1$, $\phi = 0.5$, and v_p ranging from 0 to 10. We also used 3 different values for the size of the simulation box, 50, 100 and 200, all with N = 1800. The value of the rotational diffusion coefficient is $D_\theta = 0.03$. Due to the existence of this noise term the evolution of the order parameter is not the same as what is reported in figure 4.2(a). Increasing the value of the propulsion velocity, v_p, decreased the value of t_c, seen in figure 6.1(b). This correlation between activity and synchronization time was also discussed in [25] finding similar results. This again indicates that the mobility of the oscillators is important for the synchronization process, but the fact that there does not seem to be a clear monotonous function for t_c it may indicate that some phenomena may be happening that increases the synchronization time of the system.

It was observed that before the system reaches complete synchronization a phase segregation happens where particles form aggregates, as seen in figure 6.2, where clusters of particles appear due to their collisions and different propulsion directions, a phenomena similar to motility-induce phase separation (MIPS). As particles synchronize theseclusters disappear and we no longer see them. The formation of aggregates is represented on panel (f) and (g) of figure 6.2, while no aggregate is seen when the propulsion velocity of the particles is low, $v_p = 0.1$ in panels (a) to (d) of the same figure. We speculate that if the system size was bigger we would potentially see new phenomena like density waves or separation by type of particle.

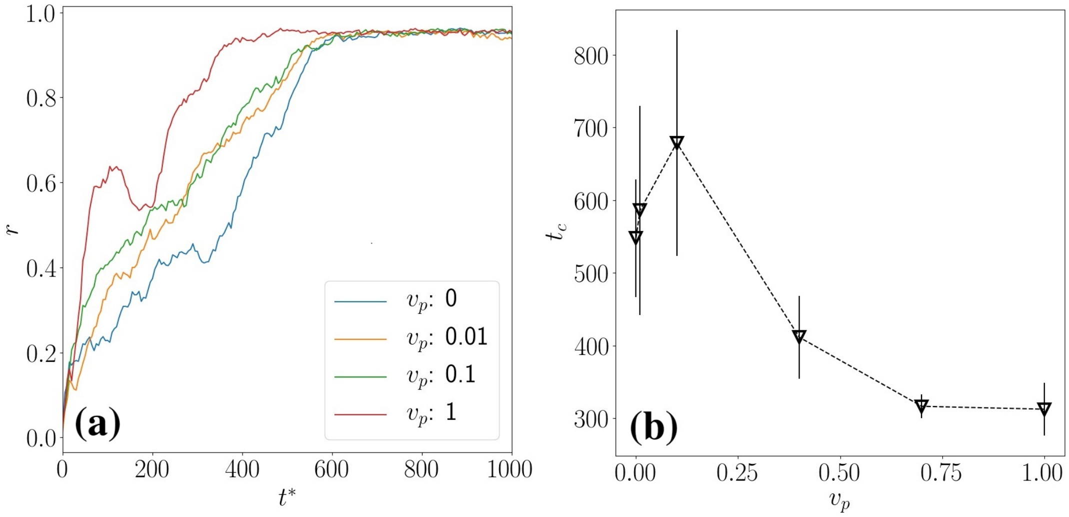

Figure 6.1: **Time evolution of the order parameter and the dependence of t_c.** Panel (a) shows the dependence of r with the value of v_p and how the activity of the particle changes the way it synchronizes, the order parameter no longer continuously growing do to existence of a rotational diffusion coefficient, D_θ. There is a non monotone dependence of t_c with v_p that may be due to the way the particles spatially distribute before synchronizing.

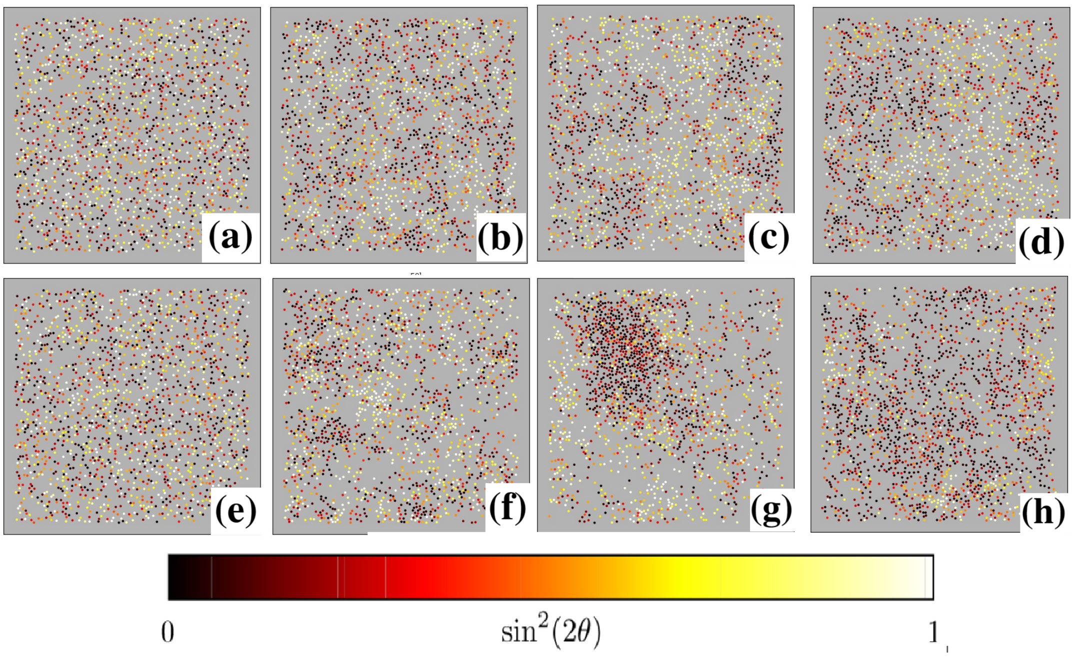

Figure 6.2: **Snapshots of clustering of active particles.** Panels (a)-(d) and (e)-(h) show the system configuration when the order parameter is 0.05, 0.30, 0.65, 0.95, respectively. We can see that in panels (a)-(d) there is no clustering, as the propulsion velocity of the particles is too low, $v_p = 0.1$. Panels (e)-(h) correspond to $v_p = 1$ and show that in intermediate times, while the system is not still synchronized, $r < 0.9$, it is possible to observe clustering . The cluster seen in (g) dissipates when the system is synchronized (h), due to the particles moving together and longer jamming together.

Chapter 7

Conclusion and future work

The study of a binary mixture of Brownian and active oscillators gave us new a understanding about the synchronization process and hints into how to control it, enhancing it or even suppressing it. We showed that if the binary mixture of oscillators behaves according to model I, synchronization cannot be suppressed but merely controlled. It can be enhanced by increasing the value of $\zeta = \frac{|H|}{K}$ and by moving the system to a state where $\phi \sim 0.5$, by increasing or decreasing the number of one type of oscillators depending on the initial system and it can be slowed down by doing the opposite, lowering the value of ζ or the fraction of repelling oscillators, shown in figures (4.3 - 4.4). Model I showed two different regimens for synchronization, if K and $|H| < 0.05$ synchronization happened according to the mean-field results, equation (2.24) and figure 4.2, and if K and $|H| > 0.05$ vortices appeared and the dynamics of synchronization changed, as can be seen in figure 4.2. For these values of $|H|$ and K there was a value of the packing fraction where τ, the late time synchronization characteristic time, was minimal, as observed in figure 4.7, as the interplay of having enough neighbouring oscillators and being able to diffuse through space conditions how fast the system synchronizes. If the binary mixture behaved like Model II it was possible to suppress synchronization by increasing the value of ζ and ϕ, as displayed in the phase diagram of figure 4.10, and an interplay between these can be used. The addition of particles of type B conditioned the synchronization of particles of type A, lowering the value of the equilibrium order parameter, r_∞. The addition of particles of type B had the same result as what was observed when the range of internal frequencies was broadened. This is a continuous configurational transition as the system goes from synchronizable to non-synchronizable as the value of ζ and ϕ increase. Finally, we explored the role of activity as an enhancer for synchronization and found that increasing activity lowers the synchronization time, and that the synchronization time saturates as the activity increases, figure 6.1. We also observed clustering of active particles, as can be seen in figure 5.3. This lead us to believe that later works on binary mixtures of active oscillators can find other kinds of collective behaviour. Future works could focus on the addition of intrinsic frequencies, ω, for the oscillators and even different distributions, $g(\omega)$, for particles of type A and B. This addition coupled with activity may display novel collective behaviour, like the separation of particles A and B due to their different chiralites, if the mean of their respective $g(\omega)$ has different signs.

Bibliography

[1] Florian Dörfler and Francesco Bullo. Synchronization in complex networks of phase oscillators: A survey. *Automatica*, 50(6):1539–1564, June 2014.

[2] F.A.S. Ferrari, R.L. Viana, S.R. Lopes, and R. Stoop. Phase synchronization of coupled bursting neurons and the generalized kuramoto model. *Neural Networks*, 66:107–118, June 2015.

[3] Hiroshi Noguchi and Masako Takasu. Self-assembly of amphiphiles into vesicles: A brownian dynamics simulation. *Physical Review E*, 64(4), 2001.

[4] Giorgio Volpe and Giovanni Volpe. Simulation of a brownian particle in an optical trap. *American Journal of Physics*, 81(3):224–230, 2013.

[5] Walter F. Paxton, Paul T. Baker, Timothy R. Kline, Yang Wang, Thomas E. Mallouk, and Ayusman Sen. Catalytically induced electrokinetics for motors and micropumps. *Journal of the American Chemical Society*, 128(46):14881–14888, 2006.

[6] Clemens Bechinger, Roberto Di Leonardo, Hartmut Löwen, Charles Reichhardt, Giorgio Volpe, and Giovanni Volpe. Active particles in complex and crowded environments. *Reviews of Modern Physics*, 88(4), 2016.

[7] Joy Adamson. *Born free: a lioness of two worlds*. Collins, 1986.

[8] Ikkyu Aihara, Hiroyuki Kitahata, Kenichi Yoshikawa, and Kazuyuki Aihara. Mathematical modeling of frogs' calling behavior and its possible application to artificial life and robotics. *Artificial Life and Robotics*, 12(1-2):29–32, March 2008.

[9] Gonzalo Marcelo Ramírez-Ávila, Jürgen Kurths, Stéphanie Depickère, and Jean-Louis Deneubourg. Modeling fireflies synchronization. In *A Mathematical Modeling Approach from Nonlinear Dynamics to Complex Systems*, pages 131–156. Springer International Publishing, June 2018.

[10] Ramon Guevara Erra, Jose L. Perez Velazquez, and Michael Rosenblum. Neural synchronization from the perspective of non-linear dynamics. *Frontiers in Computational Neuroscience*, 11, October 2017.

[11] Leon Glass. Synchronization and rhythmic processes in physiology. *Nature*, 410(6825):277–284, March (2001).

[12] O. A. Igoshin, A. Mogilner, R. D. Welch, D. Kaiser, and G. Oster. Pattern formation and traveling waves in myxobacteria: Theory and modeling. *Proceedings of the National Academy of Sciences*, 98(26):14913–14918, December 2001.

[13] Dario Antonio, David A. Czaplewski, Jeffrey R. Guest, Daniel López, Sebastián I. Arroyo, and Damián H. Zanette. Nonlinearity-induced synchronization enhancement in micromechanical oscillators. *Physical Review Letters*, 114(3), January 2015.

[14] A. A. Awad, P. Dürrenfeld, A. Houshang, M. Dvornik, E. Iacocca, R. K. Dumas, and J. Åkerman. Long-range mutual synchronization of spin hall nano-oscillators. *Nature Physics*, 13(3):292–299, November 2016.

[15] Z. Néda, E. Ravasz, T. Vicsek, Y. Brechet, and A. L. Barabási. Physics of the rhythmic applause. *Physical Review E*, 61(6):6987–6992, June 2000.

[16] J.S.Andrade Jr H.J.Herrmann V.H.P.Louzada, N.A.M.Araújo. How to suppress undesired synchronization. *Scientific Reports*, 2:658, (2012).

[17] Arkady Pikovsky. *Synchronization: Universal Concept: A Universal Concept in Nonlinear Sciences (Cambridge Nonlinear Science Series).* Cambridge University Press, (2003).

[18] D James Surmeier, Jeff N Mercer, and C Savio Chan. Autonomous pacemakers in the basal ganglia: who needs excitatory synapses anyway? *Current Opinion in Neurobiology*, 15(3):312–318, June 2005.

[19] Morten L. Kringelbach, Ned Jenkinson, Sarah L.F. Owen, and Tipu Z. Aziz. Translational principles of deep brain stimulation. *Nature Reviews Neuroscience*, 8(8):623–635, August 2007.

[20] Günther Deuschl, Carmen Schade-Brittinger, Paul Krack, Jens Volkmann, Helmut Schäfer, Kai Bötzel, Christine Daniels, Angela Deutschländer, Ulrich Dillmann, Wilhelm Eisner, Doreen Gruber, Wolfgang Hamel, Jan Herzog, Rüdiger Hilker, Stephan Klebe, Manja Kloß, Jan Koy, Martin Krause, Andreas Kupsch, Delia Lorenz, Stefan Lorenzl, H. Maximilian Mehdorn, Jean Richard Moringlane, Wolfgang Oertel, Marcus O. Pinsker, Heinz Reichmann, Alexander Reuß, Gerd-Helge Schneider, Alfons Schnitzler, Ulrich Steude, Volker Sturm, Lars Timmermann, Volker Tronnier, Thomas Trottenberg, Lars Wojtecki, Elisabeth Wolf, Werner Poewe, and Jürgen Voges. A randomized trial of deep-brain stimulation for parkinsons disease. *New England Journal of Medicine*, 355(9):896–908, August 2006.

[21] David Sumpter. *Collective animal behavior.* Princeton University Press, Princeton, N.J, 2010.

[22] Alex Arenas, Albert Díaz-Guilera, Jurgen Kurths, Yamir Moreno, and Changsong Zhou. Synchronization in complex networks. *Physics Reports*, 469:93–153, (2008).

[23] Joseph D. Skufca and Erik M. Bollt. Communication and synchronization in disconnected networks with dynamic topology: Moving neighborhood networks. *Mathematical Biosciences and Engineering*, 1(2):347–359, July 2004.

[24] Naoya Fujiwara, Jürgen Kurths, and Albert Díaz-Guilera. Synchronization in networks of mobile oscillators. *Physical Review E*, 83(2), February 2011.

[25] A. Díaz-Guilera D.Levis, I.Pagonabarraga. Synchronization in dynamical networks of locally coupled self-propelled oscillators. *Physical Review X*, 7(011028), (2017).

[26] Kevin P. O'Keeffe, Hyunsuk Hong, and Steven H. Strogatz. Oscillators that sync and swarm. *Nature Communications*, 8(1), (2017).

[27] Yoshiki Kuramoto. Lecture notes in physics, international symposium on mathematical problems in theoretical physics. *Springer-Verlag*, 39:420, (1975).

[28] Francisco A. Rodrigues, Thomas K. DM. Peron, Peng Ji, and Jürgen Kurths. The kuramoto model in complex networks. *Physics Reports*, 610:1–98, January 2016.

[29] Ruben Schmidt, Karl J. R. LaFleur, Marcel A. de Reus, Leonard H. van den Berg, and Martijn P. van den Heuvel. Kuramoto model simulation of neural hubs and dynamic synchrony in the human cerebral connectome. *BMC Neuroscience*, 16(1), September 2015.

[30] A.T. Winfree. *J. Theoret. Biol.*, 16:15, (1967).

[31] Edward Ott and Thomas M. Antonsen. Low dimensional behavior of large systems of globally coupled oscillators. 2008.

[32] Oscillator models and collective motion. *IEEE Control Systems*, 27(4):89–105, August 2007.

[33] Naomi Ehrich Leonard, Derek A. Paley, Francois Lekien, Rodolphe Sepulchre, David M. Fratantoni, and Russ E. Davis. Collective motion, sensor networks, and ocean sampling. *Proceedings of the IEEE*, 95(1):48–74, 2007.

[34] Tamás Vicsek, András Czirók, Eshel Ben-Jacob, Inon Cohen, and Ofer Shochet. Novel type of phase transition in a system of self-driven particles. *Physical Review Letters*, 75(6):1226–1229, Jul 1995.

[35] Nikolai F. Rulkov. Modeling of spiking-bursting neural behavior using two-dimensional map. *Physical Review E*, 65(4), April 2002.

[36] Paul Erdős and Alfréd Rényi. On the evolution of random graphs.

[37] Duncan J. Watts and Steven H. Strogatz. Collective dynamics of ‘small-world’ networks. *Nature*, 393(6684):440–442, June 1998.

[38] Albert-László Barabási and Eric Bonabeau. Scale-free networks. *Scientific American*, 288(5):60–69, May 2003.

[39] J. Ingen-Housz. Bemerkungen uber den gebrauch des vergr osserungsglases. *Verm. Schriftenphysisch-medicinischen Inhalts*, 1784.

[40] R. Brown. A brief account of microscopical observations made in the months of june, july and august 1827, on the particles contained in the pollen of plants; and on the general existence of active molecules in organic and inorganic bodies. *Philosophical Magazine Series 2*, 4:161–173, (1828).

[41] A. Einstein. On the motion of small particles suspended in liquids at rest required by the molecular-kinetic theory of heat. *Ann. Phys.*, 19:549, (1905).

[42] M. von Smoluchowski. Zur kinetischen theorie der brownschen molekularbewegung und der suspensionen. *Ann. Phys.*, 326:756, (1906).

[43] P. Langevin. Sur la théorie de mouvement brownien. *C. R. Hebd. Seances Acad. Sci.*, 146:530, (1908).

[44] J.B. Perrin. Mouvement brownien et réalité moléculaire. *Ann. Chim. Phys.*, 19:5, (1909).

[45] Masao Doi. *Soft Matter Physics*. Oxford University Press, aug 2013.

[46] S. Plimpton. Fast parallel algorithms for short-range molecular dynamics. *J Comp Phys*, 117(1):1–19, (1995).

[47] T. Schneider and E. Stoll. Molecular-dynamics study of a three-dimensional one-component model for distortive phase transitions. *Physical Review B*, 17(3):1302–1322, February 1978.

[48] Documentation of langevin thermostat and nve integration. `http://lammps.sandia.gov/doc/fix_langevin.html`, `http://lammps.sandia.gov/doc/fix_nve.html`.

[49] Jesse Stricker, Scott Cookson, Matthew R. Bennett, William H. Mather, Lev S. Tsimring, and Jeff Hasty. A fast, robust and tunable synthetic gene oscillator. *Nature*, 456(7221):516–519, October 2008.

[50] Tal Danino, Octavio Mondragón-Palomino, Lev Tsimring, and Jeff Hasty. A synchronized quorum of genetic clocks. *Nature*, 463(7279):326–330, January 2010.

[51] Xiao Chen, Xiang Yang, Mingcheng Yang, and H. P. Zhang. Dynamic clustering in suspension of motile bacteria. *EPL (Europhysics Letters)*, 111(5):54002, sep 2015.

[52] Alexander P. Petroff, Xiao-Lun Wu, and Albert Libchaber. Fast-moving bacteria self-organize into active two-dimensional crystals of rotating cells. *Phys. Rev. Lett.*, 114:158102, Apr 2015.